Characterization of organic aerosol across the global remote troposphere: A comparison of ATom measurements and global chemistry models

Alma Hodzic[1], Pedro Campuzano-Jost[2,3], Huisheng Bian[4], Mian Chin[4], Peter R. Colarco[4], Douglas A. Day[2,3], Karl D. Froyd[2,8], Bernd Heinold[6], Duseong S. Jo[2,3], Joseph M. Katich[2,8], John K. Kodros[5], Benjamin A. Nault[2,3], Jeffrey R. Pierce[5], Eric Ray[2,8], Jacob Schacht[6], Gregory P. Schill[2,8], Jason C. Schroder[2,3], Joshua P. Schwarz[2,8], Donna T. Sueper[2,3], Ina Tegen[6], Simone Tilmes[1], Kostas Tsigaridis[7,9], Pengfei Yu[8,10], Jose L. Jimenez[2,3]

[1]*National Center for Atmospheric Research, Boulder, CO, USA*

[2]*Cooperative Institute for Research in Environmental Sciences (CIRES), University of Colorado, Boulder, CO, USA*

[3]*Department of Chemistry, University of Colorado, Boulder, CO, USA*

[4]*NASA Goddard Space Flight Center, Greenbelt, MD, USA*

[5]*Department of Atmospheric Science, Colorado State University, Fort Collins, CO, USA*

[6]*Leibniz Institute for Tropospheric Research, Leipzig, Germany*

[7]*Center for Climate Systems Research, Columbia University, New York, NY, USA*

[8]*NOAA Earth System Research Laboratory (ESRL), Chemical Sciences Division, Boulder, CO, USA*

[9]*NASA Goddard Institute for Space Studies, New York, NY, USA*

[10]*Institute for Environmental and Climate Research, Jinan University, Guangzhou, Guangdong, China*

Key words: organic aerosol, remote atmosphere, ATom field campaign.

32 **Abstract**.

33 The spatial distribution and properties of submicron organic aerosols (OA) are among the

34 key sources of uncertainty in our understanding of aerosol effects on climate.

35 Uncertainties are particularly large over remote regions of the free troposphere and

36 Southern Ocean, where very little data has been available, and where OA predictions from

37 AeroCom Phase II global models span two to three orders-of-magnitude, greatly

38 exceeding the model spread over source regions. The (nearly) pole-to-pole vertical

39 distribution of non-refractory aerosols was measured with an aerosol mass spectrometer

40 onboard the NASA DC8 aircraft as part of the Atmospheric Tomography (ATom) mission

41 during the northern hemisphere summer (August 2016) and winter (February 2017). This

42 study presents the first extensive characterization of OA mass concentrations and their

43 level of oxidation in the remote atmosphere. OA and sulfate are the major contributors by

44 mass to submicron aerosols in the remote troposphere, together with sea salt in the marine

45 boundary layer. Sulfate was dominant in the lower stratosphere. OA concentrations have

46 a strong seasonal and zonal variability, with the highest levels measured in the lower

47 troposphere in the summer and over the regions influenced by the biomass burning from

48 Africa (up to 10 μg sm^{-3}). Lower concentrations (~0.1-0.3 μg sm^{-3}) are observed in the

49 northern mid- and high- latitudes and very low concentrations (< 0.1 μg sm^{-3}) in the

50 southern mid- and high- latitudes. The ATom dataset is used to evaluate predictions of

51 eight current global chemistry models that implement a variety of commonly used

52 representations of OA sources and chemistry, as well as of the AeroCom-II ensemble.

53 The current model ensemble captures the average vertical and spatial distribution of

54 measured OA concentrations, and the spread of the individual models remains within a

55 factor of 5. These results are significantly improved over the AeroCom-II model ensemble,

56 which shows large overestimations over these regions. However, some of the improved

57 agreement with observations occurs for the wrong reasons, as models have the tendency

58 to greatly overestimate the primary OA fraction, and underestimate the secondary fraction.

59 Measured OA in the remote free troposphere are highly oxygenated with organic aerosol

60 to organic carbon (OA/OC) ratios of ~ 2.2-2.8 and are 30-60% more oxygenated than in

61 current models, which can lead to significant errors in OA concentrations. The

62 model/measurement comparisons presented here support the concept of a more dynamic

63 OA system as proposed by Hodzic et al. (2016), with enhanced removal of primary OA,

64 and a stronger production of secondary OA in global models needed to provide a better

65 agreement with observations.

1   Introduction

Organic aerosols (OA) are a complex mixture of directly emitted primary OA (POA) and chemically produced secondary OA (SOA) from anthropogenic and biogenic emission sources. They are associated with adverse health effects (Mauderly and Chow, 2008, Shiraiwa et al., 2017) and contribute radiative forcing in the climate system (Boucher et al., 2013). The currently limited understanding of processes involved in the formation, ageing, and removal of organic compounds results in large uncertainties in (i) the predicted global OA burden, (ii) relative contributions of emissions vs. chemistry to OA formation, (iii) spatial distribution, and (iv) impacts on radiation and clouds (Kanakidou et al., 2005, Hallquist et al., 2009, Heald et al., 2011, Spracklen et al., 2011, Tsigaridis et al., 2014, Hodzic et al., 2016, Shrivastava et al., 2017, Tsigaridis and Kanakidou, 2018, Zhu et al., 2019). The uncertainties are particularly large in the estimated global burden of SOA that range from 12 to 450 Tg y^{-1} (see Fig. 9 of Hodzic et al., 2016), and in their direct and indirect radiative forcing that range from -0.08 to -0.33 W m^{-2}, and -0.60 to −0.77 W m^{-2}, respectively (Spracklen et al., 2011, Myhre et al., 2013, Scott et al., 2014, Hodzic et al., 2016, Tsigaridis and Kanakidou, 2018). Reducing these uncertainties is becoming more important as OA is on a path to becoming the dominant fraction of the submicron anthropogenic aerosol mass globally due to the ongoing efforts to reduce SO$_2$ emissions and associated sulfate aerosols.

Model performance has been especially poor in the remote regions of the atmosphere where OA measurements available for model evaluation have been sparse (especially aloft). Using data from 17 aircraft campaigns mostly located in the northern hemisphere Heald et al. (2011) showed that the skill of the global GEOS-Chem model in predicting the vertical distribution of OA was significantly decreased in remote regions compared to polluted near-source regions. The study pointed out the limitations of commonly used SOA formation mechanisms that are based on chamber data; these have the tendency to underpredict OA in source regions and overpredict OA in the remote troposphere. For a subset of 9 recent aircraft campaigns, Hodzic et al. (2016) showed that OA is likely a more dynamic system than represented in chemistry-climate models, with both stronger production and stronger removals. These authors suggested that additional removal mechanisms via e.g. photolytic or heterogeneous reactions of OA particles are needed to explain low OA concentrations observed in the upper troposphere where direct cloud scavenging is less efficient. The recent global multi-model comparison study (Tsigaridis

99   et al., 2014) within the AeroCom Phase II project illustrates well the amplitude of model
100   uncertainties simulating OA mass concentrations and the contrast in model performance
101   between near-source and remote regions. The results indicate that model dispersion (the
102   spread between the models with the lowest and highest predicted OA concentrations)
103   increases with altitude from roughly 1 order of magnitude near the surface to 2-3 orders
104   of magnitude in the upper troposphere. Our own analyses of the AeroCom-II models
105   shown in Figure 1a indicate that model dispersion (quantified as the ratio of the average
106   concentration of the highest model to that of the lowest one, in each region) increases not
107   only with altitude but also with distance from the northern mid-latitude source (and data-
108   rich) regions. The model spread is a factor of 10-20 in the free troposphere between the
109   equator and northern mid-latitudes, and increases to a factor of 200-800 over the Southern
110   Ocean and near the tropopause. It is not surprising that model spread is lower closer to
111   source regions where it is mostly driven by uncertainties in emissions and SOA production
112   yields. Spread is expected to be larger in remote regions where models are also impacted
113   by uncertainties in transport, chemical ageing and removal. The lowest model dispersion
114   also coincides with the regions of the northern hemisphere (NH) or the African biomass
115   burning outflow where models have been evaluated the most (Figure 1b), emphasizing
116   the need for further model/observation comparison studies in remote regions (of the
117   southern hemisphere (SH) in particular).

118   Here, we present a unique data set of airborne aerosol mass spectrometer measurements
119   of OA mass concentrations collected onboard the NASA DC-8 as part of the Atmospheric
120   Tomography (ATom) mission. The aircraft sampled the vertical structure of the
121   atmosphere from near-surface (0.2 km) to the lower-stratosphere (LS) regions (12 km
122   altitude) over both the Pacific and Atlantic basins (to limit the influence of source regions)
123   with a quasi-global spatial coverage from 82°N to 67°S. This dataset is used to perform
124   the first systematic global-scale multi-model evaluation of the chemistry-climate models
125   focusing on OA in the remote troposphere over the remote oceans. We focus on the NH
126   summer (August 2016, ATom-1) and NH winter (February 2017, ATom-2) deployments.
127   Overall these ATom missions sampled the marine boundary layer (MBL) for 10% of the
128   flight tracks, 12% of the time the remote lower stratosphere, and the rest the free
129   troposphere. The model-observation comparisons are aimed at identifying discrepancies
130   in terms of OA mass concentrations and vertical distribution, their fractional contribution
131   to submicron aerosols, and their oxidation level in global models.

The modeling framework is described in Section 2. Section 3 describes the ATom dataset and the spatial and vertical distributions of OA over the Atlantic and Pacific regions. Section 4 presents the comparisons of ATom-1 and -2 data to multi-model predictions from both the AeroCom-II models, and the ensemble of eight current model simulations of the ATom campaign. Section 5 presents the conclusions of the study and discusses its implications.

2   Modeling framework

2.1   ATom model simulations

ATom measurements were compared with results of eight global models that simulated the time period of the ATom-1 and 2 campaigns (August 2016 and February 2017), using the emissions and reanalysis meteorology corresponding to this period (and a spin-up time of at least six to twelve months). These are referred hereafter as ATom models and include the NASA global Earth system model GEOS5, the aerosol-climate model ECHAM6-HAM, three versions of the NCAR Community Earth System Model (CESM), and three versions of the global chemistry GEOS-Chem model. Simulations were performed at various horizontal resolutions ranging from relatively high ~50km (GEOS5) and ~100km (CESM2 models) resolutions to somewhat coarser grids of ~200km (CESM1-CARMA, GEOS-Chem) and ~400km for GC10-TOMAS. The advantage of using the same host model (in the cases of variants of CESM2 and GEOS-Chem) is that the dynamics and emissions remain comparable. Models differ greatly in their treatment of emissions, gas-phase chemistry, aerosol chemistry and physical processes, and aerosol coupling with radiation and clouds, among others. Table 1 describes the configuration of various models (e.g. meteorology, emissions), and their treatment of OA. In this section we only summarize the main features and parameters directly impacting the OA simulations. Some models do not include SOA chemistry and instead assume that SOA is directly emitted proportional to the emissions of its precursors (ECHAM6-HAM, CESM2-SMP, GEOS5, GC10-TOMAS), while others have more complex treatments of organic compounds, their chemistry, and partitioning into particles (GC12-REF, GC12-DYN, GC10-TOMAS, CESM1-CARMA, CESM2-DYN). It should be noted that models that directly emit SOA assume that SOA is a non-volatile species that remains irreversibly in the particle phase. In all models POA is treated as a non-volatile directly emitted species. In most models (see below) the primary emitted organic aerosol is artificially aged to transition between hydrophobic to hydrophilic POA. There are some commonalities between simulations for

165 the treatment of biogenic emissions, which are based in all models on the Model of
166 Emissions of Gases and Aerosols from Nature (MEGAN, Guenther et al., 2012) to
167 generate meteorology-dependent emissions of volatile organic compounds. None of the
168 models includes the marine production of OA which is estimated to be ~3 orders of
169 magnitude smaller than the continental production of OA from both isoprene and
170 monoterpene precursors (Kim et al., 2017), but could be important in the MBL. This
171 contribution could however be larger for sea-spray biological material from phytoplankton
172 with predicted contributions of 0.01 to 0.1 μg m^{-3} to surface submicron aerosol over remote
173 oceanic regions (Vergara-Temprado et al., 2017, Middlebrook et al., 1998). Below we only
174 provide a brief description of most important processes that influence OA for each model.

175 GEOS5 was run in a configuration similar to Bian et al. (2019) using the anthropogenic
176 emissions from HTAP v2 (Janssens-Maenhout et al., 2015) and biomass burning
177 emissions from the Quick Fire Emission Dataset (QFED v2.54). Aerosols are simulated
178 within the GOCART bulk aerosol module and include externally mixed particles of black
179 carbon (BC), organic carbon (OC), sulfate, ammonium, nitrate, dust and sea salt (Colarco
180 et al., 2010, Bian et al., 2017). The formation of SOA is based on a prescribed 10%
181 formation yield from the monoterpene emissions. The primary emitted OC and SOA are
182 separated into hydrophobic (50%) and hydrophilic (50%) species, with a 2.5 days e-folding
183 time conversion from hydrophobic to hydrophilic organic particles. All SOAs from biogenic,
184 anthropogenic, and biomass burning sources are treated as hydrophilic particles. Both
185 types of organic particles are dry deposited. The hydrophilic OA is removed by large-scale
186 and convective warm clouds, while hydrophobic OA is removed by ice clouds. The
187 hydrophilic particles undergo hygroscopic growth according to the equilibrium
188 parameterization of Gerber (1985).

189 The ECHAM6.3-HAM2.3 standard version (Tegen et al., 2019) was run using updated
190 anthropogenic emissions (Schacht et al, 2019) combining the ECLIPSE (Klimont et al.,
191 2017) emissions, with the Russian anthropogenic BC emissions from Huang et al. (2015).
192 For biomass burning the Global Fire Assimilation System (GFAS, Kaiser et al., 2012)
193 biomass burning emissions are used, however, without the scaling factor of 3.4 suggested
194 by Kaiser et al. (2012). Aerosol composition and processes are simulated using the
195 Hamburg Aerosol Model (HAM2, Zhang et al., 2012), that considers an aerosol internal
196 mixture of sulfate, BC, OC, sea salt, and mineral dust. The aerosol population and their
197 microphysical interactions are simulated using seven log-normal modes, including the

198   nucleation mode, soluble and insoluble Aitken, accumulation and coarse modes. In the
199   model configuration used in this publication the formation of SOA is based on a prescribed
200   15% mass yield from monoterpene emissions only (Dentener et al., 2006). Aerosol
201   particles are removed by dry and wet deposition. The wet deposition includes the below
202   cloud scavenging by rain and in-cloud cloud scavenging for large-scale and convective
203   systems (Croft et al., 2010).

204   The two simulations with the GEOS-Chem 12.0.1 global chemistry model (Bey et al.,
205   2001) use emissions based on CMIP6 global inventory (CEDS historical emissions up to
206   2014 and future emissions based on climate scenarios, Hoesly et al., 2018; Feng et al.,
207   2019) with regional improvements for anthropogenic sources, and on GFED v.4 for
208   biomass burning emissions (Giglio et al., 2013). Both simulations use the bulk aerosol
209   representation and differ only in the treatment of SOA formation and removal. The first
210   configuration   (called   hereafter   GC12-REF)   includes   the   default
211   (http://wiki.seas.harvard.edu/geos-chem/index.php) representation of SOA formation
212   based on Marais et al. (2016) for isoprene-derived SOA, and on the volatility basis set
213   (VBS) of Pye et al. (2010) for all other precursors. Note that this GEOS-Chem REF
214   simulation is similar to the version 12 default "complex option" which includes non-volatile
215   POA and semi-volatile SOA (semi-volatile POA is an optional switch within this version
216   used in Pai et al. 2020). The second configuration (referred to as GC12-DYN) includes a
217   more dynamic representation of the SOA lifecycle based on Hodzic et al. (2016), with the
218   exception of the treatment of isoprene SOA that is formed in the aqueous aerosols as in
219   Marais et al. (2016). As in Hodzic et al. (2016) the GC12-DYN model version includes
220   updated VBS SOA parameterization, updated dry and wet removal of organic vapors, and
221   photolytic removal of SOA (except for isoprene-SOA that is formed in aqueous aerosols,
222   where we follow Marais et al. 2016). SOA formation is based on wall-corrected chamber
223   yields (Zhang et al., 2014) for the traditional precursors (isoprene, monoterpenes,
224   sesquiterpenes, benzene, toluene, xylene) and on yields derived from an explicit chemical
225   mechanism for higher molecular weight n-alkanes and n-alkenes species (Hodzic et al.,
226   2016). The removal of gas-phase oxidized volatile organics uses updated Henry's law
227   solubility coefficients from Hodzic et al. (2014), and photolytic removal of SOA (Hodzic et
228   al., 2015). In addition to OA, the model includes BC and dust, and simulates the chemistry
229   and gas-particle partitioning of inorganic compounds such as sulfate, ammonium, nitrate
230   and sea salt using the ISORROPIA II thermodynamic model (Fountoukis and Nenes,
231   2007). In both GEOS-Chem configurations, BC and primary OC are simulated with a

232 hydrophobic and hydrophilic fraction for each. At the time of emission, 80% of BC and
233 50% of primary OC are considered as hydrophobic. Hydrophobic aerosols are converted
234 to hydrophilic aerosols with an e-folding lifetime of 1.15 days. An OA/OC ratio of 2.1 is
235 assumed to convert POC to POA, and SOA is simulated as OA mass (i.e. no OA/OC ratio
236 assumption is needed for SOA, except for comparison with OC measurements). Soluble
237 gases and aerosols are removed by both dry and wet deposition. Wet deposition includes
238 scavenging in convective updrafts, and in-cloud and below-cloud scavenging from large-
239 scale precipitation (Liu et al., 2001). Hydrophobic aerosols (BC and POA) are scavenged
240 in convective updrafts following Wang et al. (2014).

241 GC10-TOMAS is based on the GEOS-Chem version 10.01 coupled with TwO Moment
242 Aerosol Sectional microphysics scheme (TOMAS) and ran in a similar configuration to that
243 described in Kodros et al. (2016). The model computes the evolution of sulfate, sea salt,
244 primary and secondary OA, BC, and dust aerosols described by 15 internally mixed size
245 bins (of which six were analyzed for these comparisons, cf. Table 1). Anthropogenic
246 emissions are based on the EDGAR v4 global inventory with regional improvements, while
247 the biomass burning emissions are from GFED v3. SOA are irreversibly made from the
248 emitted parent precursor, considering a 10% mass yield from monoterpene emissions,
249 and an emission flux of 0.2 Tg of SOA per Tg of CO for the anthropogenic CO emissions.
250 The removal of gases and aerosols are treated similar to the GEOS-Chem 12.0.1 model
251 (GC12-REF, see above).

252 Simulations based on the CESM2.0 Earth system model use the standard version of the
253 Whole Atmosphere Community Climate Model (WACCM6, Gettelman et al., 2019,
254 Emmons et al., 2019). Details on the specific of the model configurations are described in
255 detail in Tilmes et al. (2019) i.e. CESM2-SMP and CESM2-DYN correspond to the
256 specified dynamics WACCM6-SOAG and WACCM6-VBSext simulations described in that
257 work, respectively. Emissions are based on the CMIP6 global inventory for the year 2014
258 for anthropogenic sources, and on the QFED version 2.4 for the wildfires inventory.
259 Aerosols are represented with the modal aerosol scheme (MAM4, Liu et al., 2012) that
260 includes BC, primary and secondary OA, sulfate, dust and sea salt. Four modes are
261 considered including Aitken, accumulation and coarse size modes, and an additional
262 primary carbon mode. Only the accumulation mode was used in this work. The CESM2-
263 SMP and CESM2-DYN simulations differ in their treatment of OA. CESM2-SMP forms OA
264 directly using fixed mass yields from primary emitted precursors (isoprene, monoterpenes,

aromatics) without explicitly simulating their oxidation and partitioning. These mass yields are increased by a factor of 1.5 to match the anthropogenic aerosol indirect forcing (Liu et al., 2012). The second configuration (referred to as CESM2-DYN) includes the formation and removal parameterizations of organics of Hodzic et al. (2016), as implemented into CESM2 by Tilmes et al. (2019) for all species based on low-NOx VBS yields only. This is a similar SOA scheme as used in GC12-DYN (with differences in the treatment of isoprene-SOA based on Marais et al. 2016 in GC12-DYN, and the use of both low- and high-NOx VBS yields in GC12-DYN). Organic gases and aerosols undergo dry and wet deposition as described in Liu et al. (2012). It should be noted that CESM2-SMP does not include deposition of intermediate organic vapors. Aerosol wet scavenging considers in-cloud scavenging (the removal of cloud-borne particles that were activated at the cloud base) and below-cloud scavenging for both convective and grid-scale clouds.

CESM1-CARMA simulations use the configuration described in Yu et al. (2019) which is based on CESM1 and the sectional Community Aerosol and Radiation Model for Atmospheres (CARMA v3.0). Anthropogenic emissions are those from the Greenhouse gas-Air pollution Interactions and Synergies (GAINS) model, and biomass burning emissions are from the Global Fire Emission Database (GFED v3, van der Werf et al., 2010). In CARMA, 20 size bins are used for both pure sulfate particles (bins from 0.2 nm to 1.3 µm in radius, only used up to 500 nm) and mixed aerosols composed of BC, primary and secondary OC, dust, sea salt, and sea-spray sulfate (bins from 0.05–8.7 µm in radius, again, only analyzed up to 500 nm). SOA formation is based on the VBS approach from Pye et al. (2010). The removal of OA occurs only by dry and wet deposition. Compared to the CESM2-SMP and CESM2-DYN simulations, the convective removal of aerosols uses the modified scheme described in Yu et al. (2019) which accounts for aerosol secondary activation from the entrained air above the cloud base, and the scavenging of activated aerosols in convective updrafts. The default CESM can transport aerosols from the cloud base to the top of the cloud in strong convective updrafts in one time step without scavenging them, while the new scheme allows for a more efficient removal off all aerosols inside convective clouds. A sensitivity simulation is performed for ATom-1 to quantify the effect of this improved removal on OA concentrations (Section 4.5).

2.2 AeroCom-II model climatology

The ATom measurements are also compared to the global model OA predictions generated within the Phase II Aerosol Comparisons between Observations and Models

298 (AeroCom-II) project (Schulz et al., 2009). We consider the monthly average results of 28
299 global models, which is a subset of those presented in Tsigaridis et al. (2014), based on
300 the availability of model results. It should be noted that the meteorological forcing used in
301 these models is mostly based on the year 2006, while the anthropogenic and biomass
302 burning emissions are mostly representative of the year 2000. For comparison purposes,
303 the monthly mean model outputs for the months of August (ATom-1) and February (ATom-
304 2) are interpolated along the flight path (latitude, longitude, and altitude), and averaged
305 the same way as the measurements (see section 3.2).

3   Description of ATom measurements

3.1   Submicron aerosol data

308 The measurements of non-refractory submicron aerosols were performed onboard the
309 NASA DC8 aircraft as part of the ATom field study (Wofsy et al., 2018) using the University
310 of Colorado Aerodyne High-Resolution Time-of-Flight Aerosol Mass Spectrometer (AMS
311 in the following, Canagaratna et al., 2007, DeCarlo et al., 2006).

312 We use measurements from both the NH summer (August 2016, ATom-1) and winter
313 (February 2017, ATom-2) deployments. Figure 2a shows the flight path and the vertical
314 extent of the ATom-1 dataset colored by OA mass concentrations (see Figure S1 for
315 ATom-2). The aircraft performed systematic vertical sampling with ~140 vertical profiles
316 per campaign throughout the troposphere from the near surface ~0.2 km to the upper
317 troposphere/lower stratosphere region at ~13 km altitude. Details on the operation of the
318 CU AMS on board the DC-8 are reported in Schroder et al. (2018), Nault et al. (2018), and
319 Jimenez et al. (2019b). AMS data was acquired at 1 Hz time resolution and independently
320 processed and reported at both 1 s and 60 s time resolutions (Jimenez et al., 2019a). The
321 later product, with more robust peak fitting at low concentrations was exclusively used as
322 the primary dataset in this work. Detection limits at different time resolutions/geographical
323 bins relevant to this study are discussed in Section 3.3. The overall 2σ accuracies of the
324 AMS measurement (38% for OA, 34% for sulfate and other inorganics) are discussed in
325 Bahreini et al. (2008) and Jimenez et al. (2019b).

326 For ATom, the AMS reported the standard non-refractory aerosol species OA, sulfate,
327 nitrate, ammonium, and chloride, with the response for all the nominally inorganic species
328 characterized by in-field calibrations. In addition, it also reported methanesulfonic acid
329 (MSA, Hodshire et al., 2019a describes the AMS MSA methods and calibrations for ATom)

330 and sea salt for for D_{geo}<450 nm (based on the method of Ovadnevaite et al., 2012). Both
331 of these species were important to achieve closure with the volume calculated from the
332 on-board sizing instruments in the marine boundary layer (Jimenez et al., 2019b). Another
333 important refractory submicron species not captured by the AMS measurements is BC.
334 This was measured on ATom with the NOAA SP2 instrument (Katich et al., 2018). It should
335 be noted that aircraft measurements of aerosol mass concentrations are given in $\mu g\ sm^{-3}$
336 (i.e., under standard conditions of 1 atm and 273.15 K).

337 For ATom the AMS measured particles with geometric diameters (based on the campaign-
338 wide average density of 1640 kg m^{-3}, Jimenez et al., 2019b) of between D_{geo}~60 and 295
339 nm with ~100% efficiency (and between 35 and 460 nm with 50% efficiency). Here we
340 denote the AMS aerosol data as "submicron" mass (based on the more usual definition
341 using aerodynamic diameter, which is larger than the geometric diameter; DeCarlo et al.,
342 2004), with the assumption that non-refractory aerosol are small contributors to mass
343 above the AMS size range. As shown in Brock et al., 2019, the accumulation mode for the
344 ATom sampling environment only extended up to 500 nm, and hence, as expected for a
345 background tropospheric environment, this approximation is appropriate. Very good
346 agreement was observed with the integrated volume calculated from the number size
347 distributions for ATom (Brock et al., 2019). A low bias compared to a typical submicron
348 definition can occur in thick biomass burning plumes and in the lower stratosphere at times
349 (Jimenez et al., 2019b). As detailed in Table 1, the accumulation mode for the bulk models
350 discussed in this study overlaps with the size range of the AMS, and for the sectional
351 models (CESM1-CARMA, GEOS-Chem-TOMAS, ECHAM6-HAM) only the bins that
352 match the AMS size range were used. As expected based on the previous discussion,
353 however, a comparison of the total OA calculated by these sectional models with the
354 modeled OA inside the AMS size-range showed small differences (Slopes for ATom-1
355 linear regressions: CESM1-CARMA:0.91, GC10-TOMAS: 0.94, ECHAM6-HAM 1.00)
356 mostly influenced by the high concentration points in the biomass plumes off Africa that
357 have a large effect on the regression since they are about 10 times larger than the bulk of
358 the dataset).

359 Refractory and non-refractory aerosol composition was also measured using the NOAA
360 Particle Analysis by Laser Mass Spectrometry (PALMS) instrument. PALMS classifies
361 individual aerosol particles into compositional classes including biomass burning (Hudson
362 et al., 2004), sea salt (Murphy et al., 2019), mineral dust (Froyd et al., 2019), and

others. Mass concentrations for these particles types are derived by combining PALMS composition data with aerosol size distribution measurements (Froyd et al., 2019). Good agreement overall was found for OA, sulfate and seasalt between the two particle mass spectrometers during ATom once the AMS and PALMS instrument transmissions were accounted for (Jimenez et al., 2019b). For all PALMS data used in this work (biomass burning fraction and dust) the AMS transmission function was applied to ensure that both instruments were characterizing approximately the same particle range.

For a particular airmass, the mass fraction of biomass burning (BB) aerosol reported by the PALMS instrument f(BB)$_{PALMS}$ (Thompson and Murphy, 2000; Froyd et al., 2019) was then used to evaluate the degree of BB influence. This parameter correlates quite well with other gas-phase BB tracers (Figure S20), and is more useful as a particle tracer since its lifetime follows that of the particles. Importantly, it is not impacted by the long lifetimes of the gas-phase tracers (e.g. 9 months for CH_3CN) and unrelated removal processes (e.g. ocean uptake for CH_3CN and HCN) that result in highly variable backgrounds. Hence f(BB)$_{PALMS}$ has a much higher contrast ratio and linearity for particle BB impacts, compared to the available gas-phase tracers in the ATom dataset. An airmass was classified as non-BB influenced when f(BB)$_{PALMS}$ was lower than 0.30 (Hudson et al, 2004) as shown in Figure 2b. For both ATom-1 and 2, about 74% of measurements were classified as not influenced by biomass burning. f(BB)$_{PALMS}$ was also used to assess the impact of POA on the total OA burden (next section); note that no thresholding was applied in that case.

3.2 Estimation of the POA fraction for the ATom dataset

For model evaluation purposes, it is important to know whether the source of OA is primary or secondary. For ground studies close to sources (e.g. Jimenez et al., 2009) Positive Matrix Factorization of AMS mass spectra (PMF, Ulbrich et al., 2009) can be used to estimate the contribution of primary sources (mostly from transportation, heating, cooking, and biomass burning) to total OA. This approach is not suitable for ATom. To accurately resolve a minor factor such as POA in an AMS dataset, there needs to be a combination of: (a) Sufficient OA mass concentration, so that the signal-to-noise of the spectra is sufficient; (b) Enough fractional mass for the factor to be resolved (>5% in urban areas per Ulbrich et al. (2009), probably a larger fraction at low concentrations such as in ATom); (c) Sufficient spatio-temporal variability ("contrast") in the relative contributions of different factors, since that is part of what PMF uses to extract the factors; (d) Sufficient difference in the spectra of the different factors (for the same reason as (c)), and (e) relatively

396 invariant spectra for each factor across the dataset (as this is a key assumption of the
397 PMF algorithm). As an example of a near ideal case, in Hodshire et al (2019) we extracted
398 MSA by PMF from the ATom-1 data, and were able to match that factor with our
399 independently calibrated MSA species. A very distinct and nearly invariant mass spectrum
400 was measured repeatedly near sources (MBL) (and was mostly absent elsewhere, thus
401 providing strong spatio-temporal contrast) and accounted for about 6% of the fractional
402 mass and 15% of the variance in time. Thus all the conditions were met. For POA, on the
403 other hand, the air sampled in ATom and coming from e.g. Asia has POA and SOA very
404 well mixed, with little change on their relative mass fractions vs. time (as the aircraft flies
405 through that airmass). POA is very low, as documented later in this paper. Atmospheric
406 aging makes the spectra from all OA sources more and more similar as measured by AMS
407 spectra (Jimenez et al., 2009). Thus most of the conditions above are not satisfied for
408 extracting POA by PMF analysis of this dataset.

409 Instead, in this work we have estimated POA based on the fact that it is co-emitted with
410 BC as part of the combustion processes releasing both species in source regions, and
411 that BC is not impacted by chemical aging processes over the lifetime of the airmass. Note
412 that BC can physically age but it is not lost in any significant amount to the gas-phase due
413 to chemical processes in the atmosphere. We assume non-differential removal (and
414 transport) of the BC fraction relative to the rest of the POA (the two are generally internally
415 mixed, Lee et al., 2015). Table S1 summarizes recent POA/BC and POC/EC emission
416 ratio determinations for urban background sites, which best represent real mixes of
417 pollution sources, and for individual sources of POA (from mobile sources – commonly
418 referred as HOA – and cooking aerosol – COA). Based on Table S1 data, we assume
419 POA to be co-emitted with BC for anthropogenic fossil fuel / urban region POA (herein
420 called FF_{ratio} for simplicity, even though much of it is non-fossil, Zotter et al., 2014; Hayes
421 et al., 2015) at a ratio of 1.5±0.82 (average ±1σ of all urban ambient air studies that report
422 POA and BC for best intercomparability to the ATom dataset; including all urban studies
423 results in a very similar number, 1.48±0.65, median: 1.41). Measurements where mobile
424 source are the main contributor in general exhibit lower ratios (POA/OA ratio 0.5-1.5),
425 while COA determination typically ranges from 2 to 3. Hence, the ratio used here is a good
426 estimate for a diverse mix of urban sources as appropriate for ATom. The studies used to
427 derive the emission ratio used ambient data in urban air, where all sources mix together
428 and impact the POA/BC ratio, and thus the ratios include the impact of POA sources that
429 may not emit BC. It should be noted that urban model ratios do not include emissions

430   associated with fugitive dust from road, tire and construction, as those are typically found
431   in larger particles than those studied here (Zhao et al., 2017). For biomass burning
432   sources, we use a value of POA/BC = 11.8 (BB_{ratio}), based on the average of the recent
433   review by Andreae (2019), which included over 200 previous determinations for a variety
434   of fuels and burning conditions (since Andreae (2019) used and OA/OC ratio of 1.6 in his
435   work, we have used that value to calculate POA/BC; we note that this is different from the
436   1.8 OA/OC ratio used for other studies listed in Table S1). We note the measured total
437   OA/BC of ~3.5 (conservatively assuming that all OA is POA) observed on both ATom
438   missions for the large African-sourced BB plumes over the Equatorial Atlantic. We note
439   that using the larger BB_{ratio} from Andreae (2019) leads to a POA fraction >> 100% in the
440   ATom African plumes. We also perform sensitivity studies with values of both FF_{ratio} and
441   BB_{ratio} within the literature range.

442   The PALMS determined mass fraction of biomass impacted aerosol ($f(BB)_{PALMS}$) can then
443   be used to determine a total POA contribution from both types of sources:

$$POA = [BC]*(FF_{ratio}+(BB_{ratio}- FF_{ratio})*f(BB)_{PALMS}) \qquad \text{(Eq. 1)}$$

445   Further detail is provided in Table S2, which summarizes the POA/BC ratios used in the
446   emission inventories implemented in current models. Overall, there is reasonable
447   agreement with the measurements in Table S1, with FF_{ratio} ranging from ~0.5 for diesel
448   fuels, to >2 for energy production and ~5 for residential emissions (which include some
449   BB). On the other hand, for biomass burning, the emission inventories ratios range from
450   ~5 for crop, to ~15 for forest, and up to ~50 for peatland. While generally consistent with
451   the values discussed by Andreae (2019), they are on the lower end of the ranges
452   discussed in that work. The averages and ranges of the measurement and model ratios
453   are similar, and thus no significant model bias on the ratios is apparent.

454   PALMS detection efficiency increases with size across the accumulation mode, and
455   therefore the f(BB) number fraction is weighted to the larger size end of the accumulation
456   mode. In very clean regions of the upper troposphere (typically <0.15 μg sm^{-3} submicron
457   mass) particles below the PALMS size range can contribute significantly to aerosol mass
458   (Williamson et al., 2019; Jimenez et al., 2019b). If BB particles are not evenly distributed
459   across the entire accumulation mode (due to preferential removal in convective updrafts
460   of primary aerosol, cf. Yu et al., 2019 and Section 4.5; and preferential condensation of
461   SOA on smaller particles), then the f(BB) reported by PALMS will be an overestimation.
462   For the final analysis these periods where left in the dataset, and therefore for the LS the

463 reported POA is likely overestimated for these regions, although their impact on the mass-
464 weighted campaign average is negligible.

465 The contribution of POA from sea spray is difficult to constrain. As an order-of-magnitude
466 estimate, marine POA is roughly calculated based on preliminary calibrations of OA on
467 mineral dust particles from the PALMS instrument (personal communication K. Froyd).
468 Using this calibration, the average OA by mass on sea salt was <10% for the large majority
469 of MBL sampling (>85%). Since sea salt contributed 4% (11%) of mass in the AMS size
470 range for ATom-1(2) (Figure 2), we estimate that marine POA is on the order of ~1% of
471 aerosol mass in the AMS size range, and possibly much lower. Thus we think that it is
472 reasonable to neglect the contribution of marine POA to this dataset. Future studies will
473 refine this estimate.

474 ### 3.3 Data processing for comparisons

475 For the comparisons between the measurements and the various global models, data
476 were averaged both vertically and zonally to minimize the impact of smaller plumes or
477 vertical gradients in aerosol concentrations that might not be captured by coarse resolution
478 models. For the same reason, all data near airports was removed from the datasets prior
479 to analysis (up to about 3 km on the climb in/out). In order to restrict this analysis to the
480 remote troposphere, the last leg of the ATom-1 mission (over the continental US) was
481 taken out of the dataset as well. Data was binned into 5 large latitude regions as shown in
482 Figure 2a including southern polar (55-80°S, "S.Polar"), southern mid-latitudes (25-55°S,
483 "S.Mid"), equatorial (25°S-25°N, "Equatorial"), northern mid-latitudes (25-55°N, "N.Mid"),
484 northern polar (55-80°N, "N.Polar") and analyzed separately for the Pacific and Atlantic
485 basins. For data in each of these latitude regions, altitude profiles were calculated with a
486 constant 600 m altitude resolution. According to both variability in the cleanest air and
487 statistical analysis of the organic background subtraction (Drewnick et al. 2009), the 1σ
488 precision at low concentrations for one-minute data ranged between 20 and 50 ng sm^{-3},
489 or a 3σ detection limit between 60 and 150 ng sm^{-3} for the one-minute data (confirmed by
490 frequent filter blanks). Per standard statistics, the precision of a measurement decreases
491 (i.e., gets better) with the square root of the number of points (or time interval) sampled.
492 I.e. the precision of an average can be approximated by the standard error of the mean
493 (σ/sqrt(n), where n is the number of measurements averaged), and it is better than the
494 precision of the individual data points (σ). This also applies to the detection limit, since it
495 is just 3 times the precision. Note that a detection limit is not meaningful unless the

496 averaging time is specified. For example let's assume that the detection limit is 20 ng m^{-3}

497 (1-second), and the data points over 60 consecutive seconds are all 10 ng m^{-3}. All 1-

498 second measurements are below the 1-second DL. However the average (10 ng m^{-3}) is

499 now above the DL for 1-minute averages, which is 20/sqrt(60) = 2.6 ng m^{-3}. On average,

500 each individual point in the profiles represents the average of about 25 min of ATom flight

501 data. At that time resolution, the OA 1σ precision was about 10 ng sm^{-3}. Hence with very

502 few exceptions (10 points for both missions combined), the OA concentrations in the

503 averaged profiles reported are well above the instrumental detection limit in those regions.

504 For model-measurement comparisons along flight tracks, model outputs and

505 measurements were considered at 1-minute time resolution, which corresponds to ~0-700

506 m vertical resolution and ~0.05-0.15 degrees horizontal resolution. Note that a large

507 fraction of the 1-minute OA values in the remote free troposphere were below the local 3σ

508 detection limit. The data of periods of zero concentration (sampling ambient air through a

509 particle filter) do average to zero. Some negative measurements are present, and this is

510 normal for measurements of very low concentrations in the presence of instrumental

511 noise. Averaging of longer periods, as done for the figures in this paper, reduces the

512 detection limit. We therefore caution future data users that the reported data should be

513 averaged as needed, as replacing below-detection limit (or negative) values by other

514 values introduces biases on averages. For fractional ratio analysis, measurements were

515 averaged to 5-minute time resolution to reduce the noise in the ratios due to noise in the

516 denominator. The results are not very sensitive to the 5-minute averaging (compared to

517 1-minute) as shown in Figure S12 for OA to sulfate ratios. The same figure also illustrates

518 that excluding ratios affected by negative concentrations (the non-bracketed case, overall

519 these are about 15% of the dataset) does not really affect the fractional distribution, with

520 the variance between the two cases diminishing as the averaging interval increases. To

521 further confirm that there is no inherent bias in the fractional products regardless of the

522 treatment of low concentration values, an additional sensitivity analysis was performed

523 where data was filtered by an independent measurement proxy for aerosol mass, the

524 aerosol volume measured in ATom (Brock et al., 2019). Using a range of value that

525 encompasses the regime where the AMS calculated volume to aerosol measured volume

526 exhibited increased noise (Jimenez et al., 2019b), no systematic bias was found (Figure

527 S13), with variations of about 10% in fractional volume for different filtering conditions.

528 Some of the performed analysis required separating the dataset into vertical subsets. In

529 this manuscript, we define the marine boundary layer (MBL) as the region below 1.5 times

the calculated boundary layer height in the NCEP global model reanalysis. The free troposphere (FT) includes all data points between the top of MBL and the NCEP tropopause height, and the LS region includes all points above the NCEP tropopause height. The tropopause height varied during ATom between 8 and 16.5 km; given the DC-8 ceiling (42 kft, 12.8 km) the stratosphere was only sampled at latitudes higher than 30 degrees in both hemispheres. The MBL height varied between up to 1.5 km in the mid-latitudes, ~1 km in the tropics, and sometimes <150 m (lowest DC-8 altitude) for some of the sampling in the polar troposphere.

3.4 Submicron aerosol composition

Figure 2b shows that during both NH summer and winter ATom deployments, OA is one of the three dominant components of the measured submicron aerosol in the remote troposphere, together with sulfate and sea salt. During ATom-1, average submicron aerosol concentrations were close to 0.8 μg sm^{-3} in the marine boundary layer and biomass burning outflow regions, and ~2 times lower in the free troposphere and lower stratosphere regions. ATom-2 had overall lower average concentrations below 0.4 µg sm^{-3} (vs. 0.5 µg sm^{-3} for ATom-1). As expected, sulfate (sulfuric acid in the lower stratosphere) is the dominant constituent in the MBL (~50%) and LS (50-70%), while the OA contribution is generally below 10% and 40%, respectively in those regions. A large fraction of sea salt aerosol is found in the MBL especially during the NH winter deployment (~30%, see Murphy et al., 2019).

OA is found to be a major constituent (~50%) of submicron aerosol in the clean (non-BB influenced) free troposphere. The contribution of OA is 1.4 times larger than that of sulfate during the NH summer, and 1.2 times lower than that of sulfate during the NH winter, which is likely due to a large contribution of the NH sources to SOA production in the NH summer. Biomass-burning events increase the OA contribution relative to that of sulfate, and lead to a higher contribution of OA to total during the ATom-1 mission (stronger BB influence).

3.5 Spatial and vertical distribution of OA

Figure 2a (and Fig. S1) shows the spatial and vertical distribution of OA mass concentrations measured during ATom-1 (and ATom-2) campaigns. Most data were taken over remote oceanic regions (and a few remote continental regions, primarily over the Arctic). The measured OA varies between extremely clean conditions (< 0.1 µg sm^{-3})

562   encountered mostly in the Pacific and Southern Ocean regions and moderately polluted
563   conditions (> 2 µg sm^{-3}) in the biomass burning outflow regions. During ATom-1 (August
564   2016), a strong BB influence is observed in the lower troposphere (below 6 km) over the
565   Atlantic basin off the African coast and over California with OA concentrations exceeding
566   10 µg sm^{-3}. OA associated with biomass burning is also present in the upper troposphere
567   over equatorial regions and over Alaska, associated with the deep convective transport of
568   biomass burning aerosols. The biomass burning contribution to carbonaceous aerosols in
569   those regions during ATom-1 was also apparent in the black carbon measurements
570   (Katich et al., 2019). ATom-2 was generally less polluted than ATom-1, likely due to a
571   more limited global influence of biomass burning emissions during that period, and also to
572   a less active photochemistry during winter months in the NH.

573   The measured OA is characterized by a strong latitudinal gradient. Figure 2c shows the
574   average vertical profiles of measured OA over the selected latitudinal bands during August
575   2016. The cleanest airmasses are observed over the remote oceanic regions of the
576   Southern Hemisphere (SH, 25-80°S) with OA mass concentrations below 0.06 µg sm^{-3}.
577   These extremely low OA concentrations can be explained by the very low influence from
578   continental emission sources, and presumably low marine POA and SOA precursor
579   emissions. This is consistent with low concentrations of gas-phase pollutants (e.g. CO,
580   ethane, propane). An enhancement can be noticed above 10 km in the lower stratosphere.
581   In some cases, this could be related to the long-range transport of biomass burning
582   aerosols from the tropics. By comparison, the Arctic region is more polluted with an order
583   of magnitude higher OA levels compared to its analog of the SH (i.e. OA loadings ranging
584   from 0.1 to 0.5 µg sm^{-3}). These concentrations are comparable to FT levels measured in
585   the extratropical regions (25-55°N) of the NH. The equatorial marine regions (25°S-25°N)
586   display the highest OA concentrations with a strong gradient between lower and upper
587   troposphere. In the lower troposphere OA, concentrations are close to 1 µg sm^{-3}, and
588   decrease down to 0.1 µg sm^{-3} at altitudes above 4km. The highest OA levels are
589   associated with the African outflow over the southeastern Atlantic Ocean, which results
590   from the transport of the biomass burning smoke from the sub-Saharan regions and
591   increasing urban and industrial air pollution in southern West Africa (Flamant et al., 2018).
592   Figure 2d shows that the Atlantic basin is often more polluted than the Pacific basin, not
593   only because of the African biomass burning influence but also due to the contribution of
594   anthropogenic pollution in the lower troposphere of the NH. It should be noted that Asian

595   pollution was likely an important contributor to the North Pacific Basin, especially between

596   2 and 6 km, in both ATom deployments (see figures 2a and S1). Several-fold higher OA

597   concentrations are found near the surface (below 1km) over the southern Pacific

598   compared to that same location in the southern Atlantic, which could be indicative of the

599   stronger emission of marine OA in the Pacific basin.

600   In addition to spatial gradients, a strong summer-to-winter contrast is observed in OA

601   concentrations. Figure 2e shows the ratio between OA vertical profiles measured in the

602   NH summer ATom-1 vs. in the NH winter ATom-2. The NH is more polluted during the NH

603   summer due to the photochemical production of SOA, as well as biomass burning

604   emissions, leading to the tripling of OA concentrations in the extratropical regions (25-

605   80°N) on average regardless of altitude. The doubling of OA loading in the lower

606   troposphere at the equator (25°S-25°N) in the NH summer (August, ATom-1) is strongly

607   influenced by the biomass burning activity in the sub-Saharan African region as already

608   mentioned above. Likewise, OA concentrations are found to be generally higher in the SH

609   during the SH summer. These zonal trends are broadly similar to the ones described in

610   Katich et al (2018) for BC.

611   **4   Model-measurement comparisons**

612   ***4.1   Evaluation of predicted OA concentrations***

613   Prior to evaluating model performance in simulating OA, we have assessed the ATom

614   models' ability to simulate sulfate aerosols. According to the model evaluation shown in

615   Table S3, the predicted sulfate concentrations are generally within 40% of the measured

616   values, which is comparable to the AMS measurement uncertainties. The only exception

617   is found for the ECHAM6-HAM model, which overestimates sulfate aerosols by a factor of

618   two. These results imply that most ATom models capture relatively well the overall sulfate

619   burden. However, large root mean square error (RMSE > 0.4 µg sm^{-3} for ATom-1 and >

620   0.2 µg sm^{-3} for ATom-2) is indicative of their limited skill in reproducing the observed

621   variability in sulfate concentrations.

622   For OA, model evaluation metrics for the entire ATom-1 and ATom-2 campaigns are given

623   in Table 2 for the eight ATom models and their ensemble, as well as the AeroCom-II

624   ensemble. The results show that the normalized mean bias is substantially lower for the

625   ATom model ensemble compared to AeroCom-II decreasing from 74% to 4% for ATom-1

626   and from 137% to 23% to ATom-2, which is within the measurement uncertainty range.

627 The mean temporal correlations are substantially improved from 0.31 (0.38) for AeroCom-
628 II to 0.66 (0.48) for ATom model ensemble during ATom-1 (ATom-2). However, results
629 vary strongly among ATom models. Models using prescribed emissions of non-volatile
630 SOA have the tendency to overestimate the OA concentrations during both NH summer
631 and winter deployments (with ~35-60% overestimation for CESM2-SMP, ~70-100% for
632 ECHAM6-HAM, and up to 150% for GC10-TOMAS during ATom-2), with the exception of
633 the GEOS5 model that on the contrary underestimates OA concentrations by 5-25%.
634 During the NH summer (ATom-1), models using the VBS parameterization from Pye et al.
635 (2010) tend to underpredict the OA concentrations by 43% for GC12-REF and 33% for
636 CESM1-CARMA for ATom-1, most likely due to the excessive evaporation of the formed
637 SOA in remote regions and low yields for anthropogenic SOA (Schroder et al., 2018; Shah
638 et al., 2019). Models using the VBS parameterization from Hodzic et al. (2016) (CESM2-
639 DYN and GC12-DYN) where OA is less volatile and also OA yields are corrected for wall
640 losses show an improved agreement with observations especially for CESM2-DYN (with
641 NMB of ~5%), and to a lesser extent for GC12-DYN (NMB of ~33%). During the NH winter
642 (ATom-2) characterized by a lower production of SOA, both VBS approaches lead to an
643 overestimation of the predicted OA. This is likely caused by excessively high levels of
644 primary emitted OA as discussed in section 4.4.

645 Figure 3 compares the average median ratios between modeled and observed OA
646 concentrations for the ATom and AeroCom-II model ensembles for different regions (BB,
647 MBL, FT, LS). The results show that the median ratio for the ATom model ensemble is
648 close to unity in all regions. This is at least a factor of two improvement compared to
649 AeroCom-II models, which were almost always biased high for the remote regions
650 sampled in ATom. The model spread has also been reduced by a factor of 2-3 in all
651 regions. This reduction in the ensemble spread may partially be explained by a smaller
652 size of the ATom model ensemble (see Fig. S2), which also includes models with a more
653 up-to-date OA representation. In order to explore this point further, results for a subset of
654 AeroCom-II models (using earlier versions of models in the ATom ensemble) show only a
655 slight reduction (~10%) in the model spread, with however some regional differences i.e.
656 an improved agreement with observations in the MBL, but an increase in the model bias
657 and spread in the LS (Figure S2). Thus, model improvement for the more recent models
658 appears to be the main reason for the reduced spread.

4.2   Evaluation of predicted OA vertical distribution

Figure 4 compares the mean vertical profiles of OA measured during ATom-1 and -2 with the predictions of the model ensemble average based on the eight ATom models (Table 1) and 28 AeroCom-II models for the different latitudinal regions of the Pacific and Atlantic basins. Note that the use of a wide logarithmic scale (to be able to span all the observations) may make the observed differences appear small, although they often reach factors of 2-10 and larger (Figure S5 shows the results on a linear scale). For AeroCom-II, large latitudinal differences exist in the results with a better performance closer to source regions and large disagreement in the lower stratosphere and remote regions, as already suggested by the mission medians shown in Figure 3. The best AeroCom-II model performance is found over the equator in both basins, where the model ensemble captures within a factor of 2 the observed OA concentrations throughout the troposphere in the Pacific basin, and matches remarkably well the observations in the lower troposphere of the Atlantic basin that is heavily influenced by biomass burning emissions. Reasonable agreement is found for the OA vertical distribution over the NH Atlantic and Pacific oceans, especially in the lower troposphere (< 4 km). The largest model discrepancies (1-2 orders of magnitude) are found in the remote regions of the Southern Ocean and SH mid-latitudes during both seasons and basins. The model overestimation is also large over the NH mid-latitude Pacific basin in the upper troposphere. A spread of 2-3 orders of magnitude is observed around the ensemble average indicating a very large variability in individual model predictions. This evaluation of AeroCom-II models in remote regions is an extension of that performed at the surface for urban and remote stations by Tsigaridis et al. (2014) (as in that previous study, the data and model simulations compared are not synchronous in time). The tendency of the model ensemble to overpredict OA concentrations by a factor of 2 on average in the remote regions is consistent with the transition from the large underprediction in OA near the source region to a slight overprediction of OA in remote continental sites that was reported for most AeroCom-II models (Tsigaridis et al., 2014), and also observed for default parameterizations in other studies (Heald et al., 2011; Hodzic et al., 2016).

By comparison, the results of the ATom model ensemble show a much better agreement with observations. The model spread is still substantial, but mostly below a factor of 5. Figures S6 and S7 show OA vertical profiles for individual ATom models and the spread in their results. In most regions, the ATom model ensemble captures reasonably well both

the absolute concentrations as well as the shape of the vertical profiles. In the biomass burning outflow and NH mid-latitude regions, the ATom ensemble average better captures the higher OA concentrations in the boundary layer and lower OA concentrations in the lower stratosphere than the AeroCom-II ensemble. We note that using the ensemble median OA profiles instead of ensemble mean OA profiles (as shown in Figure 5 and S7) results in a slightly lower values of OA but does not change the conclusions of the model-measurement comparisons (Figure S18).

4.3 Oxidation level of organic aerosols (OA/OC ratios)

In addition to OA mass concentrations, we also evaluate the model's ability to simulate their degree of oxygenation, an indicator of their oxidation and aging (Aiken et al., 2008; Kroll et al., 2011). Ambient measurements of the oxidation level of organic particles are limited (Aiken et al., 2008, Canagaratna et al., 2015), and the ATom dataset provides the first global distribution of O/C and OA/OC ratios for the remote aerosol. The OA/OC ratio is an estimate of the average molecular weight of organic matter per carbon weight, and it mostly depends on the oxygen content (i.e. the O/C ratio), in the absence of significant concentrations of organonitrates and -sulfates. It is needed to compare measurements of organic aerosol mass (from e.g. AMS) with organic carbon measurements (from e.g. thermooptical methods). It is also needed to compare the various types of measurements to model concentrations, which are sometimes carried internally as OA and sometimes as OC. A low OA/OC ratio is indicative of freshly emitted OA from fossil fuel combustion (typically ~1.4), and its value increases with increased processing of organics in the atmosphere. Figure 5 shows that in the remote regions the bulk of measured OA/OC ratios during ATom-1 and -2 range between 2.2 and 2.5, and are larger than values of 2.1 $\pm$ 0.2 found in the polluted US continental outflow regions that were sampled during SEAC4RS, WINTER and DC3 field campaigns (Schroder et al., 2018). These values indicate that remote OA is highly oxidized and chemically processed.

Note that for organosulfates ($R-O-SO_2H$ and organonitrates ($R-O-NO_2$, $pRONO_2$ in the following) only one oxygen is included in the reported OA/OC, as the fragments of these species are typically the same as for inorganic species in the AMS (Farmer et al., 2010). However in ATom organosulfates are estimated to account for ~1% of the total sulfate (based on PALMS data, see Liao et al., 2015 for the methodology). Since sulfate and OA concentrations are comparable, organosulfates would only increase the OA/OC by ~1% on average. Organonitrates are reported from the AMS for ATom. Their impact on OA/OC

725 is not propagated for the default values, to maintain consistency with a large set of OA/OC

726 measurements by AMS in the literature, and since they would increase OA/OC on average

727 by only 4.5% (ATom-1) and 2.2% (ATom-2), which is smaller than the uncertainty of this

728 measurement. However, we show the results with both methods in Fig. 5 to fully document

729 this topic.

730 Importantly, this ratio is also used to calculate the total OA mass concentration for models

731 that provided their outputs in terms of organic carbon concentrations ($[OA]_i = [OC]_i$ x

732 OA/OC_{ratio}). Most Models use a constant OA/OC ratio, but the value used varies

733 substantially. OA/OC of 1.4 is used in ECHAM6-HAM, whereas 1.8 is used in GEOS5 and

734 GC10-TOMAS simulations for both POA and SOA. Other models calculated directly SOA

735 concentrations without applying this conversion (CESM1-CARMA, CESM2-SMP, CESM2-

736 DYN, GC12-REF and GC12-DYN), but for POA used the ratio of 1.8 (CESM1-CARMA,

737 CESM2-SMP, CESM2-DYN) and 2.1 (GC12-REF and GC12-DYN). Most of the AeroCom-

738 II models used the ratio of 1.4 for all primary and secondary OA (Tsigaridis et al., 2014).

739 The comparison with measurements shows that the measured values are ~40% larger

740 than those assumed in some of the ATom models, and 60-80% larger than used in

741 AeroCom-II models. The comparison between the observed and predicted OA/OC vertical

742 profiles (Fig. S3) shows that AeroCom-II models tend to generally underpredict this ratio,

743 and do not capture its increase in remote regions. As a result, this underestimation of

744 OA/OC ratios and the use of a constant value could substantially impact the comparisons

745 of OA mass concentrations for several models considered in this study (ECHAM6-HAM,

746 GEOS5, CESM1-CARMA and GC10-TOMAS). If we correct for the underestimated

747 OA/OC ratio using the ATom measured values of 2.2 (to be conservative) and compare

748 to previously discussed biases in Table 2, the overprediction of the ECHAM6-HAM model

749 is increased to ~110-160%, and that of GC10-TOMAS to 180% during ATom-2 while

750 having ~15% bias in ATom-1, whereas GEOS5 results now overestimate up to 30% during

751 ATom1, and perform much better during ATom-2.

752 These results demonstrate that current global chemistry-climate models use unrealistically

753 low OA/OC ratios, which results in a large underestimate of the degree of oxidation of OA

754 in remote regions. Inaccurate prediction of OA oxidation as it ages could impact not only

755 the calculations of OA burden, but also its optical properties as the absorption of OA

756 changes with its degree of oxidation (through the formation and destruction of brown

757 carbon, Laskin et al., 2015, Forrister et al., 2015). However, models used in this study did
758 not include these effects.

4.4 Contribution of primary vs. secondary OA

760 We further assess whether global models can adequately predict the relative contributions
761 of primary and secondary OA. We strive to quantify these fractions with the most
762 straightforward methods (with the fewest assumptions) for both models and
763 measurements. POA concentrations were estimated from the BC measurements by using
764 an emission ratio appropriate to the airmass origin (biomass burning vs. anthropogenic),
765 as quantified by the f(BB) mass fraction from the PALMS single particle instrument (see
766 Section 3.2), with f(BB)=1 taken as a BC and OA being of pure BB airmass origin and
767 f(BB)=0 exclusively from a non-biomass burning source. By using the POA/BC ratio at the
768 source regions after most evaporation, but before POA chemical degradation evaporation
769 has taken place, we implicitly assume POA to be chemically inert, while in reality it can
770 slowly be lost to the gas-phase by heterogeneous chemistry (e.g. George and Abbatt,
771 2010; Palm et al., 2018). Thus, the observation-based method provides an upper limit to
772 the fraction of POA. The model/measurement comparison is only shown for the CESM
773 and GEOS-Chem model variants, as other participating models do not separate or did not
774 report their POA and SOA fractions. In all simulations, POA was treated as a chemically
775 inert directly emitted primary aerosol species that only undergoes transport,
776 transformation from hydrophobic to hydrophilic state with ageing (1-2 days typically),
777 coagulation, and dry and wet deposition. Importantly, the treatment of POA as non-volatile
778 (rather than semi-volatile) in models is fully consistent with the assumptions for POA
779 estimation from the measurements.

780 Figure 6 compares the vertical profiles of measurement-derived POA during ATom-1 and
781 predicted by the CESM2-DYN model over clean remote regions of the Pacific basin and
782 northern polar Atlantic that are not influenced by biomass burning. Comparisons for other
783 models are similar (not shown). Observations show that POA is extremely small in remote
784 regions, whereas the model predicts that about half of the OA is made of POA in those
785 areas. Although the model reproduces quite well the measured total OA, it tends to
786 severely overpredict the amount of POA and underpredict that of SOA over clean remote
787 regions (with the two errors canceling each other when it comes to total OA). Over the
788 biomass burning regions (not shown here) it can be difficult to directly quantify POA and
789 SOA with this method, as total OA remains about constant, while POA decreases with

790   aging and SOA increases (Cubison et al., 2011; Jolleys et al., 2015; Hodshire et al.,
791   2019b). However, given this evolution the method used here would lead to an
792   overestimate of POA for this reason.

793   A more general comparison is made in Figure 7, using the frequency distributions of the
794   measured and simulated fraction of POA/OA, for the free troposphere only (Figure S8
795   shows the corresponding cumulative distributions). Observations indicate that most
796   remote FT airmasses contain less than 10% POA, except for biomass burning plumes that
797   are considered mostly primary. A slightly higher proportion of POA is seen in ATom-2,
798   which is consistent with a slower photochemical production of SOA during NH winter.
799   These results indicate that the remote OA is consistently dominated by SOA regardless
800   of the season and location. The comparison with models reveals a very large discrepancy
801   in the predicted vs. measured POA vs. SOA contributions. Models have a general
802   tendency to severely overpredict the fraction of POA and underpredict that of SOA,
803   displaying a much wider frequency distribution than the measurements (as also shown for
804   POA and SOA vertical profiles for individual models on Figures S6 and S7). In GC12-REF,
805   CESM2-DYN and CESM1-CARMA (without improved in-cloud removal) predictions for
806   ATom-1, more than a half of the remote OA is POA, while that is very rarely observed in
807   the free troposphere (possibly only during strong biomass burning events). Most models
808   fail to reproduce the overwhelming dominance of SOA that is inferred from the
809   measurements during ATom-1, while the discrepancies are less severe during NH winter
810   (ATom-2). These seasonal differences suggest that model errors could be partially due to
811   inefficient production of SOA and/or too high POA emissions, although removal errors also
812   probably play a major role (see next section).

813   The differences are so large that they are pretty insensitive to details of the POA estimation
814   method from the measurements, mostly because for the vast majority of the ATom track
815   BC/OA ratios were extremely low and hence the exact magnitude of the multiplicative
816   factor is secondary to the estimation of POA (Figure S11). As Figure S9 illustrates, the
817   choice of FF_{ratio} has very little impact on the overall distribution of POA. On the other hand,
818   while the BB_{ratio} does impact the overall distribution of POA, it mostly affects the points in
819   the vicinity of the large Atlantic plumes. Since the POA/BC ratio in those plumes is fairly
820   low, (see Section 3.2), using a very large BB_{ratio} mostly leads to an increase of the fraction
821   of the points where POA > 100%. While the large range of published BB_{ratio} for different
822   sources precludes a more accurate estimation by our method, for the purposes of the

823 comparison with the model results we emphasize that even using the largest BB_{ratio},
824 fraction of SOA is still significantly larger in the ATom dataset that in any of the models.

825 Additional sensitivity tests were performed to investigate the impact of noisy data and
826 uncertainties of f(BB) on the estimation of POA. Figure S11 clearly shows that the impact
827 of a misattribution of the aerosol type by the stated PALMS uncertainty (Froyd et al., 2019)
828 is completely negligible. Figure S10 details how the choice of averaging interval (with
829 longer averaging times reducing both the fraction of OA measurements under the DL and
830 below zero) impact the distribution of POA. Overall, no large changes are observed for
831 averaging times >5 min, and hence a 5 min averaging interval was used for the analysis
832 in Figure 7. Figure S10 also illustrates how capping the histogram impacts the POA
833 distribution. To capture the most realistic $f_{(POA)}$ distribution, the data in Fig 7 was capped
834 at the extremes (so $f_{(POA)}<0$ is taken as $f_{(POA)}=0$, and $f_{(POA)}>1$ is taken as $f_{(POA)}=1$). As Figure
835 S10 shows, data with $f_{(POA)}<0$ is almost exclusively due to very small (and always positive,
836 since BC cannot go negative) POA values being divided by small, negative noise in total
837 OA, and hence treating that fraction of the histogram as essentially fPOA~0 is justified.
838 On the other end of the distribution, data where POA is larger than OA is mostly due to
839 our average BB_{ratio} being larger than the one encountered in most of the BB plumes in
840 ATom. Choosing a lower BB_{ratio}, as Figures S9b and S9d illustrate, leads to $f_{(POA)}>1$
841 basically trending to zero, confirming our interpretation. This is a limitation of the dataset,
842 and it does not seem appropriate to remove these points, since some fraction are likely
843 dominated by POA. However, it shows that the POA estimation, especially for this part of
844 the distribution likely overstates the importance of POA.

845 A comparison between simulations that have the same treatment of POA, and only differ
846 in their chemistry and removal of SOA (e.g. CESM2-SMP vs. CESM2-DYN; GC12-REF
847 vs. GC12-DYN) indicate that a more complex SOA treatment does not always result in a
848 more accurate simulation of the primary/secondary character of OA, a result that was also
849 found in the AeroCom-II multi-model intercomparison (Tsigaridis et al., 2014).

850 Finally, we have examined whether the non-volatile treatment of POA in models could
851 lead to these unrealistically high POA fractions in the remote regions. Figure S16 shows
852 a comparison of POA vertical profiles as predicted by the GC12-REF simulations that use
853 non-volatile POA and a sensitivity simulation GC12-REF-SVPOA that uses semi-volatile
854 POA similar to the standard treatment in GEOS-Chem as described in Pai et al. (2020).
855 Note, however, that Pai et al. (2020) included marine POA emissions, used different

856 reanalysis meteorology, and a different model version (12.1.1 rather than 12.0.1 here), so
857 their resulting comparisons to ATom measurements are somewhat different than found
858 here for GC12-REF-SVPOA. The comparison indicates that the POA concentrations
859 increase substantially in most regions when the semi-volatile POA parameterization is
860 used. These results suggest that non-volatile treatment of POA is not responsible of the
861 model bias.

862 ### *4.5   Sensitivity to OA formation and removal*

863 In this section, we further investigate some of the possible reasons for the incorrect model
864 predictions of the relative contributions of POA and SOA in remote regions. Given the
865 tendency of models to underestimate OA close to anthropogenic source regions and
866 overestimate OA downwind in past studies (e.g. Heald et al., 2011; Tsigaridis et al., 2014;
867 Hodzic et al., 2016), in this section we investigate the sensitivity of OA to increasing
868 sources and increasing removals. We have performed two additional model simulations
869 to test the sensitivity of the POA/SOA fractions to uncertainties in the representation of (i)
870 wet scavenging, based on the CESM1-CARMA simulations in which we have removed
871 the improvements in the aerosol removal by the convective updrafts (Yu et al., 2019); and
872 of (ii) SOA formation based on the GC12-REF simulations in which we have replaced the
873 SOA formation VBS mechanism (Pye et al., 2010) by an updated VBS mechanism that
874 uses chamber wall-loss corrected SOA yields (Hodzic et al., 2016, same formation
875 scheme that is used in GC12-DYN and CESM2-DYN runs, but with removals kept identical
876 to GC12-REF). The results of these two sensitivity simulations are displayed on Figure 8,
877 which shows measured and predicted mass concentrations of OA, POA, SOA and sulfate
878 for ATom-1 as a function of the number of days since the air mass was processed through
879 convection. One should keep in mind that this is an averaged plot that included airmasses
880 from various regions and altitudes, and not a Lagrangian plot following the same airmass.

881 ***Sensitivity to in-cloud scavenging in convective clouds.*** Inefficient wet removal of
882 primary OA could contribute to the POA overprediction in global models, especially in the
883 tropics. Previous global model studies have reported two to three orders of magnitude
884 overestimation of primary carbonaceous species such as BC in the free troposphere when
885 the removal in the convective updrafts was not included (e.g. Schwarz et al., 2013, Yu et
886 al., 2019). A strong reduction due to convective removal is also expected for POA
887 concentrations, as POA is a primary species co-emitted with BC at the surface and
888 internally mixed with it (Lee et al., 2015), and that is typically coated by secondary

889   inorganics and organics over short timescales (Petters et al., 2006; Jiang et al., 2010;
890   Wang et al., 2010). Figures 7a and 8 compare the simulations of CESM1-CARMA with
891   and without improved convective in-cloud scavenging during ATom-1. The improved in-
892   cloud scavenging scheme considers aerosol activation into cloud droplets from entrained
893   air above the cloud base, which is more realistic and results in a more efficient removal of
894   aerosols in the upper troposphere by convection. E.g. a two order of magnitude reduction
895   in BC in the upper FT was reported by Yu et al. (2019), resulting in much improved
896   agreement with observations. Similar results were observed for sea salt aerosols in
897   Murphy et al. (2019). Figure 8 shows that all submicron aerosol species simulated in
898   CESM1-CARMA are strongly impacted by the in-cloud removal above the cloud base.
899   POA concentrations are reduced by an order of magnitude while sulfate is reduced by
900   30% leading in both cases to a much-improved agreement with observations. SOA is
901   reduced by ~30% as well, which leads to an underprediction of measured SOA
902   concentrations. The overall impact on OA concentrations is a significant reduction, which
903   leads to ~20% underestimation of OA in the aged remote air during ATom-1.

904   For the CESM2-DYN model that does not have improved in-cloud removal, the reasonable
905   agreement (within 20%) with the observed OA concentrations thus results from
906   coincidental error compensation between the overpredicted POA and underpredicted
907   SOA. The prescribed SOA formation and the artificial 50% adjustment of SOA emissions
908   based on Liu et al. (2012) in CESM2-SMP leads to an overestimation of observed SOA in
909   aged remote airmasses.

910   ***Sensitivity to SOA formation.*** In addition, we have also tested the sensitivity of the OA
911   composition to the choice of the SOA formation mechanism. Figure 8 compares the results
912   of the GC12-REF model that uses SOA formation yields derived from traditional chamber
913   experiments (Pye et al., 2010) and those corrected for loses of organic vapors onto
914   chamber walls as proposed in Hodzic et al. (2016). Previous studies have reported that
915   chamber wall losses could lead up to a factor of 4 underprediction of formed SOA (Zhang
916   et al., 2014; Krechmer et al., 2016). It should be noted that in both cases, isoprene-SOA
917   is formed in aqueous aerosols following Marais et al. (2016). The comparison shows a
918   factor of 3 increase in SOA concentrations when the updated SOA formation is considered
919   leading to a much better agreement with the observed SOA as well as the observed total
920   OA. GC12-REF predicts well the amount of POA and overpredicts somewhat the amount
921   of sulfate aerosols, which is expected as it already includes the improved aerosol removal

922   in convective updrafts (Wang et al., 2014). Figure S6 also shows that POA vertical
923   distribution is well captured in GEOS-Chem in most regions, except over the polar north
924   Pacific. It should be noted that these results are consistent with the POA/OA frequency
925   distribution shown in Figure 7 (the POA/OA ratio predicted by GC12-REF is larger than
926   the measured ratio, which is consistent with the fact that POA is about the right amount,
927   and OA is underpredicted in Figure 8).

928   These sensitivity simulations suggest that a stronger convective removal of POA and a
929   stronger production of SOA might be needed to correctly represent not only the total OA
930   concentrations but also its primary and secondary nature in remote free troposphere and
931   remote ocean regions. Accurate predictions of the OA concentration, composition, and
932   source contributions for the right reasons are key for accurately predicting their lifecycle
933   and radiative impacts. Only when there is confidence that the sources are accurately
934   predicted, we can have confidence in OA predictions for pre-industrial and future
935   conditions, as well as to evaluate PM mitigation strategies.

4.6   OA and sulfate relative contributions in FT

937   Finally, we assess the model ability to predict relative amounts of OA and sulfate in the
938   free troposphere where they are the two major constituents of the submicron aerosol
939   (Figure 2b). Accurate predictions of their relative contributions are crucial to determine the
940   hygroscopicity of the submicron aerosol, and its ability to serve as a cloud condensation
941   nuclei (CCN) in the remote free troposphere (Carslaw et al., 2013; Brock et al., 2016).

942   Figure 9a compares the average measured relative fractions of sulfate (36%) and
943   carbonaceous aerosols (OA=59% and BC=5%) in the FT with those predicted by
944   individual models during ATom-1. The CESM2 models best reproduce the observed
945   relative contributions, with a slight underestimation of OA (57% instead of 59%) for
946   CESM2-DYN, and a slight overestimation of OA (63% instead of 59%) for CESM2-SMP.
947   GEOS5 has 15% more OA relative to sulfate than observed. All other models
948   underestimate both OA and BC relative fractions. For instance, in GC12-REF and -DYN,
949   both the BC and OA fractions are ~40% (relative) lower than observed.

950   Figure 9b shows the frequency distribution of observed and predicted fractions of OA
951   relative to sulfate during ATom-1 and -2 in the free troposphere. Most models fail to
952   reproduce the relatively uniform nature of the observed distributions during ATom-1, with
953   typically narrower model shapes around a preferred ratio. The NH summer measurements

954   indicate that OA > sulfate in ~55% of the samples (consistent with Fig. 2b), while models

955   generally tend to underestimate the relative OA contribution. In particular, GEOS-Chem

956   and ECHAM6-HAM tend to overestimate the relative contribution of sulfate. A better

957   agreement is found for GEOS5, CESM1-CARMA and CESM2-DYN, which follow more

958   closely the shape of the observed distribution. The comparisons also suggest that the

959   more complex SOA treatment of SOA formation and removal proposed by Hodzic et al.

960   (2016) in the same host model leads to an improved agreement with observations (e.g.

961   CESM2-DYN vs. CESM2-SMP; GC12-DYN vs. GC12-REF). It should be noted that

962   CESM2-SMP uses fixed SOA yields that were increased by 50% as suggested by Liu et

963   al. (2012), leading to an overestimation of the relative contribution of OA compared to that

964   of sulfate in the free troposphere. During the NH winter (ATom-2), measurements show a

965   somewhat higher proportion of sulfate aerosols (vs. ATom-1), which is consistent with a

966   slower production of SOA in the NH during winter and a reduced influence of biomass

967   burning. Similar conclusions are found for the evaluation of different models. It is worth

968   mentioning that the comparison performed for the whole ATom-1 and 2 dataset (not

969   shown) leads to similar results with even slightly stronger overestimation of the sulfate

970   relative contribution compared to OA.

971   The discrepancies between the observed and predicted composition of submicron aerosol

972   over remote regions can be quite large for other constituents as well. Figure 10 shows the

973   comparison of measured and predicted composition of the submicron aerosol over the

974   Southern Ocean (during the NH winter) where the disagreement in simulated sea salt,

975   nitrates, ammonium, and MSA often exceeds the contribution of OA. While the

976   observations show a more uniform distribution of non-marine aerosol with higher values

977   in the mid and upper troposphere, respectively, most models tend to simulate highest

978   fractions of OA (and sulfate) towards the tropopause. This may also be explained by the

979   uncertainties in modeled wet removal of aerosol that has been discussed above. Specific

980   studies have discussed and continue to investigate the ATom measurements and

981   simulations of different components in more detail, including particle number (Williamson

982   et al., 2019), black carbon (Katich et al., 2018; Ditas et al., 2019), MSA (Hodshire et al.,

983   2019), sulfate-nitrate-ammonium (Nault et al., 2019), and sea salt (Yu et al, 2019; Bian et

984   al., 2019; Murphy et al., 2019).

985

5 Conclusions and implications

Our understanding and representation in global models of the lifecycle of the OA remain highly uncertain, especially in remote regions where constraints from measurements have been very sparse. We have performed a systematic evaluation of the performance of eight global chemistry climate models and of 28 AeroCom-II models in simulating the latitudinal and vertical distribution of OA and its composition in the remote regions of the Atlantic and Pacific marine boundary layer, free troposphere and lower stratosphere, using the unique measurements from the ATom campaign. Our simulations are conducted for both ATom-1 and ATom-2 deployments that took place in August 2016 and February 2017, respectively. The main conclusions of the comparison are as follows:

- The AeroCom-II ensemble average tends to be biased high by a factor of 2-5 in comparison to measured vertical OA profiles in the remote atmosphere during both NH summer and NH winter. The ensemble spread increases from a factor of 40 in the NH source regions to a factor of 1000 in remote regions of the Southern Ocean. The evaluation of AeroCom-II models in the remote regions provides an extension of the previous evaluation with continental ground data by Tsigaridis et al. (2014). We note that the data from the AeroCom-II models were based on monthly mean values from a different simulated year than the ATom campaigns; however, the consistent model biases are strong enough that we would not expect our conclusions to change for a different modeled year.

- The results of the ATom model ensemble used in this work show a much better agreement with the OA observations in all regions and reduced model variability. However, some of the agreement is for the wrong reasons, as most models severely overestimate the contribution of POA and underestimate the contribution of SOA to total OA. Sensitivity simulations indicate that the POA overestimate in CESM could be due to an inadequate representation of primary aerosol removal by convective clouds, (additional convective removal per Yu et al. (2019) in CESM1-CARMA led to a better agreement with observations). Most models have insufficient production of SOA, and sensitivity studies indicate that a stronger production of SOA is needed to capture the measured concentrations. The photochemical ageing of POA which was not considered here (unlike for SOA) could also contribute to the model overestimation. The non-volatile POA treatment in models is consistent with the assumption of inert POA particles used to estimate POA from measurements, and cannot explain the

1019   model bias. Indeed, sensitivity simulations with semi-volatile POA lead to a much
1020   larger model bias for OA in the upper troposphere and remote regions. The
1021   compensation between errors in POA and SOA in remote regions is however a
1022   recurring issue in OA modeling (de Gouw and Jimenez, 2009). For instance, it was
1023   found in the urban outflow regions such as Mexico City during MILAGRO 2006 field
1024   campaign (Fast et al., 2009; Hodzic et al., 2009); Paris during MEGAPOLI 2009
1025   (Zhang et al., 2013); the Los Angeles area during CalNex-2010 (Baker et al., 2015;
1026   Woody et al., 2016); the NE US outflow during WINTER 2015 (Schroder et al., 2018;
1027   Shah et al., 2019).

1028   • Additional errors in simulated OA concentrations can arise from the use of too low
1029   OA/OC ratios when model results (often calculated as OC) are converted to OA for
1030   comparison with measurements. We note that OA is the most atmospherically-relevant
1031   quantity, while OC is an operational quantity, partially a relic from a period in which
1032   only OC could be separately quantified (although also of some use for carbon budget
1033   studies). It should also be noted that most emission inventories still use OC as the
1034   primary variable, which is why the use of accurate OA/OC ratios is still key for all
1035   models. We show that the OA/OC ratio used in most models is too low compared to
1036   measured values that range mostly from 2.2 to 2.5, resulting in errors in OA mass of
1037   ~70% for AeroCom-II models and ~30% for current models that use organic carbon to
1038   track OA mass. Remote OA is thus highly oxidized and chemically processed. These
1039   results demonstrate that current global chemistry-climate models underestimate the
1040   degree of oxidation of OA in remote regions and need to consider further chemical
1041   ageing of OA, which could impact the calculations of its burden, and optical and
1042   hygroscopic properties.

1043   • The results also show that in most models (except CESM2) the predicted OA
1044   contribution to the total submicron aerosol is underestimated relative to sulfate in the
1045   remote FT where OA and sulfate are the dominant submicron aerosols (important for
1046   climate). Accurate predictions of composition of submicron particles remains
1047   challenging in remote regions and should be the topic of future studies.

1048   Key implications of our results are: (i) Model errors on the relative contribution of POA and
1049   SOA to OA reduce our confidence on the ability to simulate radiative forcing over time or
1050   OA health impacts; (ii) Model errors for the relative contributions of sulfate and organics
1051   to the submicron aerosol in the free troposphere could lead to errors in the predicted CCN
1052   or radiative forcing of aerosols as inorganics are more hygroscopic than OA; (iii) the OA

system seems to be more dynamic with a need for an enhanced removal of primary OA, and a stronger production of secondary OA in global models to provide a better agreement with observations.

Acknowledgements. The authors want to thank the ATom leadership team and the NASA logistics and flight crew for their contributions to the success of ATom. Authors acknowledge Dr. Rebecca Buchholz (NCAR) for providing the emissions used for the CESM2 simulations. We thank C. Brock and C. Williamson (NOAA) for the aerosol volume data, Paul Wennberg (Calthech) for HCN data and Eric Apel and Rebecca Hornbrook (NCAR) for CH_3CN data used in Fig, S20. The ATOM measurements and analyses were supported by NASA grants NNX15AH33A, NNX15AJ23G, and 80NSSC19K0124. AH was supported by the National Center for Atmospheric Research, which is operated by the University Corporation for Atmospheric Research on behalf of the National Science Foundation. JRP and JKK were supported by the US Department of Energy's Atmospheric System Research, an Office of Science, Office of Biological and Environmental Research program, under grant no. DE-SC0019000. This project has received support from the European Research Council under the European Union's Horizon 2020 research and innovation programme (grant agreement No. 819169), and from EPA STAR grant 83587701-0. This manuscript has not been reviewed by EPA, and no endorsement should be inferred. We would like to acknowledge high-performance computing support from Cheyenne provided by NCAR's Computational and Information Systems Laboratory. We thank C. Brock for the aerosol volume data, and D. Murphy for useful discussions. We thank the ATom leadership team, science team and the NASA DC-8 crew for their contributions to the success of the ATom mission.

Code/Data availability: Data can be obtained from the ATom website: https://doi.org/10.3334/ORNLDAAC/1581.

L2 Measurements from CU High-Resolution Aerosol Mass Spectrometer (HR-AMS) can be obtained from the ORNL DAAC, Oak Ridge, Tennessee, USA. https://doi.org/10.3334/ORNLDAAC/1716.

Author contribution: A. Hodzic, P. Campuzano-Jost and J.L. Jimenez performed the measurement / model comparisons, wrote and revised the manuscript. P. Campuzano-Jost, D.A. Day, B.N. Nault, J.C. Schroder, D.T. Sueper, and J. L. Jimenez performed and analyzed the AMS measurements. K.D. Froyd and G.P. Schill performed and analyzed the PALMS measurements. J.P. Schwarz and J.M. Katich performed the BC

measurements. H. Bian, M. Chin, P.R. Colarco, B. Heinold, A. Hodzic, D.S. Jo, J.K. Kodros, J.R. Pierce, E. Ray, J. Schacht, I. Tegen, S. Tilmes, K. Tsigaridis, and P. Yu provided model output. All authors provided comments on the manuscript.

References

Aiken, A.C., P.F. DeCarlo, J.H. Kroll, D.R. Worsnop, J.A. Huffman, K. Docherty, I.M. Ulbrich, C. Mohr, J.R. Kimmel, D. Sueper, Q. Zhang, Y. Sun, A. Trimborn, M. Northway, P.J. Ziemann, M.R. Canagaratna, T.B. Onasch, R. Alfarra, A.S.H. Prevot, J. Dommen, J. Duplissy, A. Metzger, U. Baltensperger, and J.L. Jimenez. O/C and OM/OC Ratios of Primary, Secondary, and Ambient Organic Aerosols with High Resolution Time-of-Flight Aerosol Mass Spectrometry Environmental Science & Technology, 42, 4478–4485, doi: 10.1021/es703009q, 2008.

Andreae, M. O.: Emission of trace gases and aerosols from biomass burning – An updated assessment, Atmos. Chem. Phys. Discuss., 1–27, doi:10.5194/acp-2019-303, 2019.

Bahreini, R., Ervens, B., Middlebrook, A. M., Warneke, C., de Gouw, J. A., DeCarlo, P. F., Jimenez, J. L., Brock, C. A., Neuman, J. A., Ryerson, T. B., Stark, H., Atlas, E., Brioude, J., Fried, A., Holloway, J. S., Peischl, J., Richter, D., Walega, J., Weibring, P., Wollny, A. G. and Fehsenfeld, F. C.: Organic aerosol formation in urban and industrial plumes near Houston and Dallas, Texas, J. Geophys. Res., 114, D00F16, doi:10.1029/2008JD011493, 2009.

Baker, K. R., Carlton, A. G., Kleindienst, T. E., Offenberg, J. H., Beaver, M. R., Gentner, D. R., Goldstein, A. H., Hayes, P. L., Jimenez, J. L., Gilman, J. B., de Gouw, J. A., Woody, M. C., Pye, H. O. T., Kelly, J. T., Lewandowski, M., Jaoui, M., Stevens, P. S., Brune, W. H., Lin, Y.-H., Rubitschun, C. L., and Surratt, J. D.: Gas and aerosol carbon in California: comparison of measurements and model predictions in Pasadena and Bakersfield, Atmos. Chem. Phys., 15, 5243-5258, https://doi.org/10.5194/acp-15-5243-2015, 2015.

Bey, I., Jacob, D. J., Yantosca, R. M., and Logan, J. A.: Global modeling of tropospheric chemistry with assimilated meteorology: model description and evaluation, J Geophys. Res., 106, 23073–23095, 2011.

Bian, H., Froyd, K., Murphy, D. M., Dibb, J., Chin, M., Colarco, P. R., Darmenov, A., da Silva, A., Kucsera, T. L., Schill, G., Yu, H., Bui, P., Dollner, M., Weinzierl, B., and Smirnov, A.: Observationally constrained analysis of sea salt aerosol in the marine atmosphere, Atmos. Chem. Phys. Discuss., https://doi.org/10.5194/acp-2019-18, 2019.

1118   Bian, H., Chin, M., Hauglustaine, D. A., Schulz, M., Myhre, G., Bauer, S. E., Lund, M. T.,
1119   Karydis, V. A., Kucsera, T. L., Pan, X., Pozzer, A., Skeie, R. B., Steenrod, S. D., Sudo, K.,
1120   Tsigaridis, K., Tsimpidi, A. P., and Tsyro, S. G.: Investigation of global nitrate from the
1121   AeroCom Phase III experiment, Atmos. Chem. Phys., 17, 12911-12940,
1122   https://doi.org/10.5194/acp-17-12911-2017, 2017.

1123   Boucher, O., D. Randall, P. Artaxo, C. Bretherton, G. Feingold, P. Forster, V.-M.
1124   Kerminen, Y. Kondo, H. Liao, U. Lohmann, P. Rasch, S.K. Satheesh, S. Sherwood, B.
1125   Stevens and X.Y. Zhang: Clouds and Aerosols. In: Climate Change 2013: The Physical
1126   Science Basis. Contribution of Working Group I to the Fifth Assessment Report of the
1127   Intergovernmental Panel on Climate Change [Stocker, T.F., D. Qin, G.-K. Plattner, M.
1128   Tignor, S.K. Allen, J. Boschung, A. Nauels, Y. Xia, V. Bex and P.M. Midgley (eds.)].
1129   Cambridge University Press, Cambridge, United Kingdom and New York, NY, USA, 2013.

1130   Bowman, K. P.: Large-scale isentropic mixing properties of the Antarctic polar vortex from
1131   analyzed winds. J. Geophys. Res., 98 (D12), 23 013–23 027, 1993.

1132   Brock, C. A., Wagner, N. L., Anderson, B. E., Attwood, A. R., Beyersdorf, A., Campuzano-
1133   Jost, P., Carlton, A. G., Day, D. A., Diskin, G. S., Gordon, T. D., Jimenez, J. L., Lack, D.
1134   A., Liao, J., Markovic, M. Z., Middlebrook, A. M., Ng, N. L., Perring, A. E., Richardson, M.
1135   S., Schwarz, J. P., Washenfelder, R. A., Welti, A., Xu, L., Ziemba, L. D., and Murphy, D.
1136   M.: Aerosol optical properties in the southeastern United States in summer – Part 1:
1137   Hygroscopic growth, Atmos. Chem. Phys., 16, 4987-5007, https://doi.org/10.5194/acp-16-
1138   4987-2016, 2016.

1139   Brock, C. A., Williamson, C., Kupc, A., Froyd, K. D., Erdesz, F., Wagner, N., Richardson,
1140   M., Schwarz, J. P., Gao, R.-S., Katich, J. M., Campuzano-Jost, P., Nault, B. A., Schroder,
1141   J. C., Jimenez, J. L., Weinzierl, B., Dollner, M., Bui, T. and Murphy, D. M.: Aerosol size
1142   distributions during the Atmospheric Tomography Mission (ATom): methods,
1143   uncertainties, and data products, Atmos. Meas. Tech., 12(6), 3081–3099,
1144   doi:10.5194/amt-12-3081-2019, 2019.

1145   Canagaratna, M. R., Jayne, J. T., Jimenez, J. L., Allan, J. D., Alfarra, M. R., Zhang, Q.,
1146   Onasch, T. B., Drewnick, F., Coe, H., Middlebrook, A. M., Delia, A., Williams, L. R.,
1147   Trimborn, A. M., Northway, M. J., DeCarlo, P. F., Kolb, C. E., Davidovits, P., and Worsnop,
1148   D. R.: Chemical and microphysical characterization of ambient aerosols with the Aerodyne

Aerosol Mass Spectrometer, Mass Spectrom. Rev., 26, 185–222, https://doi.org/10.1002/mas.20115, 2007.

Canagaratna, M. R., Jimenez, J. L., Kroll, J. H., Chen, Q., Kessler, S. H., Massoli, P., Hildebrandt Ruiz, L., Fortner, E., Williams, L. R., Wilson, K. R., Surratt, J. D., Donahue, N. M., Jayne, J. T., and Worsnop, D. R.: Elemental ratio measurements of organic compounds using aerosol mass spectrometry: characterization, improved calibration, and implications, Atmos. Chem. Phys., 15, 253-272, https://doi.org/10.5194/acp-15-253-2015, 2015.

Carslaw, K. S., Lee, L. a, Reddington, C. L., Pringle, K. J., Rap, A., Forster, P. M., Mann, G. W., Spracklen, D. V, Woodhouse, M. T., Regayre, L. a and Pierce, J. R.: Large contribution of natural aerosols to uncertainty in indirect forcing., Nature, 503(7474), 67–71, doi:10.1038/nature12674, 2013.

Colarco, P., da Silva, A., Chin, M., and Diehl, T.: Online simulations of global aerosol distributions in the NASA GEOS-4 model and comparisons to satellite and ground based aerosol optical depth, J. Geophys. Res., 115, D14207, doi:10.1029/2009JD012820, 2010.

Croft, B., Lohmann, U., Martin, R. V., Stier, P., Wurzler, S., Feichter, J., Hoose, C., Heikkilä, U., van Donkelaar, A., and Ferrachat, S.: Influences of in-cloud aerosol scavenging parameterizations on aerosol concentrations and wet deposition in ECHAM5-HAM, Atmos. Chem. Phys., 10, 1511–1543, https://doi.org/10.5194/acp-10-1511-2010, 2010.

Cubison, M. J., Ortega, A. M., Hayes, P. L., Farmer, D. K., Day, D., Lechner, M. J., Brune, W. H., Apel, E., Diskin, G. S., Fisher, J. A., Fuelberg, H. E., Hecobian, A., Knapp, D. J., Mikoviny, T., Riemer, D., Sachse, G. W., Sessions, W., Weber, R. J., Weinheimer, A. J., Wisthaler, A., and Jimenez, J. L.: Effects of aging on organic aerosol from open biomass burning smoke in aircraft and laboratory studies, Atmos. Chem. Phys., 11, 12049-12064, https://doi.org/10.5194/acp-11-12049-2011, 2011.

DeCarlo, P., Slowik, J., Worsnop, D., Davidovits, P., Jimenez, J., Stainken, K., Williams, L., Jayne, J., Kolb, C. and Rudich, Y.: Particle Morphology and Density Characterization by Combined Mobility and Aerodynamic Diameter Measurements. Part 1: Theory, Aerosol Sci. Technol., 38(12), 1185–1205, doi:10.1080/027868290903907, 2004.

DeCarlo, P. F., Kimmel, J. R., Trimborn, A., Northway, M. J., Jayne, J. T., Aiken, A. C., Gonin, M., Fuhrer, K., Horvath, T., Docherty, K. S., Worsnop, D. R., and Jimenez, J. L.:

Field-Deployable, High-Resolution, Time-of-Flight Aerosol Mass Spectrometer, Anal. Chem., 78, 8281–8289, https://doi.org/10.1021/ac061249n, 2006.

de Gouw, J., and J.L. Jimenez. Organic Aerosols in the Earth's Atmosphere. Environmental Science & Technology, 43, 7614–7618, 2009. DOI: 10.1021/es9006004

Dentener, F., Kinne, S., Bond, T., Boucher, O., Cofala, J., Generoso, S., Ginoux, P., Gong, S., Hoelzemann, J. J., Ito, A., Marelli, L., Penner, J. E., Putaud, J.-P., Textor, C., Schulz, M., van der Werf, G. R., and Wilson, J.: Emissions of primary aerosol and precursor gases in the years 2000 and 1750 prescribed data-sets for AeroCom, Atmospheric Chemistry and Physics, 6, 4321–4344, https://doi.org/10.5194/acp- 6-4321-2006, https://www.atmos-chem-phys.net/6/4321/2006/, 2006.

Ditas, J., Ma, N., Zhang, Y., Assmann, D., et al.: Strong impact of wildfires on the abundance and aging of black carbon in the lowermost stratosphere, Proc. Natl. Acad. Sci., 811595-11603, doi:10.1073/pnas.1806868115, 2018.

Drewnick, F., Hings, S. S., Alfarra, M. R., Prevot, A. S. H. and Borrmann, S.: Aerosol quantification with the Aerodyne Aerosol Mass Spectrometer: detection limits and ionizer background effects, Atmos. Meas. Tech., 2(1), 33–46, 2009.

Emmons, L. K., Orlando, J. J., Tyndall, G., Schwantes, R. H., Kinnison, D. E., Marsh, D. R., Mills, M. J., Tilmes, S., and Lamarque, J.-F.: The MOZART Chemistry Mechanism in the Community Earth System Model version 2 (CESM2), to be Submitted to J. Adv. Modeling Earth Systems, 2019.

Farmer, D.K., A. Matsunaga, K.S. Docherty, J.D. Surratt, J.H. Seinfeld, P.J. Ziemann, and J.L. Jimenez. Response of an Aerosol Mass Spectrometer to Organonitrates and Organosulfates and implications for Atmospheric Chemistry. Proceedings of the National Academy of Sciences of the USA, 107, 6670-6675, doi: 10.1073/pnas.0912340107, 2010.

Fast, J., Aiken, A. C., Allan, J., Alexander, L., Campos, T., Canagaratna, M. R., Chapman, E., DeCarlo, P. F., de Foy, B., Gaffney, J., de Gouw, J., Doran, J. C., Emmons, L., Hodzic, A., Herndon, S. C., Huey, G., Jayne, J. T., Jimenez, J. L., Kleinman, L., Kuster, W., Marley, N., Russell, L., Ochoa, C., Onasch, T. B., Pekour, M., Song, C., Ulbrich, I. M., Warneke, C., Welsh-Bon, D., Wiedinmyer, C., Worsnop, D. R., Yu, X.-Y., and Zaveri, R.: Evaluating simulated primary anthropogenic and biomass burning organic aerosols during MILAGRO: implications for assessing treatments of secondary organic aerosols, Atmos. Chem. Phys., 9, 6191-6215, https://doi.org/10.5194/acp-9-6191-2009, 2009.

1213   Feng, L., Smith, S. J., Braun, C., Crippa, M., Gidden, M. J., Hoesly, R., Klimont, Z., van

1214   Marle, M., van den Berg, M., and van der Werf, G. R.: Gridded Emissions for CMIP6,

1215   Geosci. Model Dev. Discuss., https://doi.org/10.5194/gmd-2019-195, in review, 2019.

1216   Flamant, C., Knippertz, P., Fink, A. H., Akpo, A., Brooks, B., Chiu, C. J., Coe, H., Danuor,

1217   S., Evans, M., Jegede, O., Kalthoff, N., Konaré, A., Liousse, C., Lohou, F., Mari, C.,

1218   Schlager, H., Schwarzenboeck, A., Adler, B., Amekudzi, L., Aryee, J., Ayoola, M.,

1219   Batenburg, A. M., Bessardon, G., Borrmann, S., Brito, J., Bower, K., Burnet, F., Catoire,

1220   V., Colomb, A., Den- jean, C., Fosu-Amankwah, K., Hill, P. G., Lee, J., Lothon, M.,

1221   Maranan, M., Marsham, J., Meynadier, R., Ngamini, J.-B., Rosenberg, P., Sauer, D.,

1222   Smith, V., Stratmann, G., Taylor, J. W., Voigt, C., and Yoboué, V.: The Dynamics-Aerosol-

1223   Chemistry- Cloud Interactions in West Africa field campaign: Overview and research

1224   highlights, B. Am. Meteorol. Soc., 99, 83–104, https://doi.org/10.1175/BAMS-D-16-

1225   0256.1, 2018.

1226   Forrister, H., Liu, J., Scheuer, E., Dibb, J., Ziemba, L., Thornhill, K. L., Anderson, B.,

1227   Diskin, G., Perring, A. E., Schwarz, J. P., Campuzano-Jost, P., Day, D. A., Palm, B. B.,

1228   Jimenez, J. L., Nenes, A. and Weber, R. J.: Evolution of brown carbon in wildfire plumes,

1229   Geophys. Res. Lett., 42(11), doi:10.1002/2015GL063897, 2015.

1230   Fountoukis, C. and Nenes, A.: ISORROPIA II : a computationally efficient thermodynamic

1231   equilibrium model for K^+-Ca^{2+}-Mg^{2+}-Na^+-SO_4^{2-}-NO_3^--Cl^--H_2O aerosols, Atmos. Chem.

1232   Phys., 7, 4639–4659, 2007.

1233   Froyd, K. D., Murphy, D. M., Brock, C. A., Campuzano-Jost, P., Dibb, J. E., Jimenez, J.-

1234   L., Kupc, A., Middlebrook, A. M., Schill, G. P., Thornhill, K. L., Williamson, C. J., Wilson,

1235   J. C., and Ziemba, L. D.: A new method to quantify mineral dust and other aerosol species

1236   from aircraft platforms using single particle mass spectrometry, Atmos. Meas. Tech.

1237   Discuss., https://doi.org/10.5194/amt-2019-165, in review, 2019.

1238   George, I. J. and Abbatt, J. P. D.: Heterogeneous oxidation of atmospheric aerosol

1239   particles by gas-phase radicals, Nature Chemistry, 2, 713–722, 2010.

1240   Gettelman, A., Mills, M. J., Kinnison, D. e., Garcia, R. R., Smith, A. K., Marsh, D. R.,

1241   Tilmes, S., Vitt, F., Bardeen, C. G., McInerny, J., Liu, H.-L., Solomon, S. C., Polvani, L.

1242   M., Emmons, L. K., Lamarque, J.-F., Richter, J. H., Glanville, A. S., Bacmeister, J. T.,

1243   Phillips, A. S., Neale, R. B., Simpson, I. R., DuVivier, A. K., Hodzic, A., Randel, W. J.: The

1244   Whole Atmosphere Community Climate Model Version 6 (WACCM6), J. of Geophys. Res.,
1245   in review, 2019.

1246   Gerber, H. E.: Relative-humidity parameterization of the Navy Aerosol Model (NAM),
1247   Tech. Rep. NRL Report 8956, Naval Research Laboratory, 1985.

1248   Giglio, L., Randerson, J. T. and Werf, G. R.: Analysis of daily, monthly, and annual burned
1249   area using the fourth-generation global fire emissions database (GFED4), J. Geophys.
1250   Res. Biogeosciences, 118, 317–328, 2013.

1251   Guenther, A. B., Jiang, X., Heald, C. L., Sakulyanontvittaya, T., Duhl, T., Emmons, L. K.,
1252   and Wang, X.: The Model of Emissions of Gases and Aerosols from Nature version 2.1
1253   (MEGAN2.1): an extended and updated framework for modeling biogenic emissions,
1254   Geosci. Model Dev., 5, 1471–1492, https://doi.org/10.5194/gmd-5-1471-2012,
1255   https://www.geosci-model-dev.net/5/1471/2012/, 2012.

1256   Hayes, P. L., Carlton, A. G., Baker, K. R., Ahmadov, R., Washenfelder, R. A., Alvarez, S.,
1257   Rappenglück, B., Gilman, J. B., Kuster, W. C., de Gouw, J. A., Zotter, P., Prévôt, A. S. H.,
1258   Szidat, S., Kleindienst, T. E., Offenberg, J. H., Ma, P. K., and Jimenez, J. L.: Modeling the
1259   formation and aging of secondary organic aerosols in Los Angeles during CalNex 2010,
1260   Atmos. Chem. Phys., 15, 5773-5801, https://doi.org/10.5194/acp-15-5773-2015, 2015.

1261   Hallquist, M., Wenger, J. C., Baltensperger, U., Rudich, Y., Simpson, D., Claeys, M.,
1262   Dommen, J., Donahue, N. M., George, C., Goldstein, A. H., Hamilton, J. F., Herrmann, H.,
1263   Hoffmann, T., Iinuma, Y., Jang, M., Jenkin, M. E., Jimenez, J. L., Kiendler-Scharr, A.,
1264   Maenhaut, W., McFiggans, G., Mentel, Th. F., Monod, A., Prévôt, A. S. H., Seinfeld, J. H.,
1265   Surratt, J. D., Szmigielski, R., and Wildt, J.: The formation, properties and impact of
1266   secondary organic aerosol: current and emerging issues, Atmos. Chem. Phys., 9, 5155-
1267   5236, https://doi.org/10.5194/acp-9-5155-2009, 2009.

1268   Heald, C. L., Coe, H., Jimenez, J. L., Weber, R. J., Bahreini, R., Middlebrook, A. M.,
1269   Russell, L. M., Jolleys, M., Fu, T.-M., Al- lan, J. D., Bower, K. N., Capes, G., Crosier, J.,
1270   Morgan, W. T., Robinson, N. H., Williams, P. I., Cubison, M. J., DeCarlo, P. F., and Dunlea,
1271   E. J.: Exploring the vertical profile of atmospheric organic aerosol: comparing 17 aircraft
1272   field campaigns with a global model, Atmos. Chem. Phys., 11, 12673–12696,
1273   doi:10.5194/acp-11-12673-2011, 2011.

1274   Hodshire, A. L., Campuzano-Jost, P., Kodros, J. K., Croft, B., Nault, B. A., Schroder, J.
1275   C., Jimenez, J. L. and Pierce, J. R.: The potential role of methanesulfonic acid (MSA) in

1276 aerosol formation and growth and the associated radiative forcings, Atmos. Chem. Phys.,
1277 19(5), 3137–3160, doi:10.5194/acp-19-3137-2019, 2019a.

1278 Hodshire, A., A. Akherati, M. Alvarado, B. Brown-Steiner, S. Jathar, J.L. Jimenez, S.
1279 Kreidenweis, C. Lonsdale, T. Onasch, A. Ortega, J. Pierce. Aging Effects on Biomass
1280 Burning Aerosol Mass and Composition: A Critical Review of Field and Laboratory
1281 Studies. Environ. Sci. Technol., submitted, 2019b.

1282 Hodzic, A., Jimenez, J. L., Madronich, S., Aiken, A. C., Bessagnet, B., Curci, G., Fast, J.,
1283 Lamarque, J.-F., Onasch, T. B., Roux, G., Schauer, J. J., Stone, E. A., and Ulbrich, I. M.:
1284 Modeling organic aerosols during MILAGRO: importance of biogenic secondary organic
1285 aerosols, Atmos. Chem. Phys., 9, 6949-6981, https://doi.org/10.5194/acp-9-6949-2009,
1286 2009.

1287 Hodzic, A., Aumont, B., Knote, C., Lee-Taylor, J., Madronich, S., and Tyndall, G.: Volatility
1288 dependence of Henry's law constants of condensable organics: Application to estimate
1289 depositional loss of secondary organic aerosols, Geophys. Res. Lett., 41, 4795–4804,
1290 doi:10.1002/2014GL060649, 2014.

1291 Hodzic, A., Madronich, S., Kasibhatla, P. S., Tyndall, G., Aumont, B., Jimenez, J. L., Lee-
1292 Taylor, J., and Orlando, J.: Organic photolysis reactions in tropospheric aerosols: effect
1293 on secondary organic aerosol formation and lifetime, Atmos. Chem. Phys., 15, 9253-9269,
1294 https://doi.org/10.5194/acp-15-9253-2015, 2015.

1295 Hodzic, A., Kasibhatla, P. S., Jo, D. S., Cappa, C. D., Jimenez, J. L., Madronich, S., and
1296 Park, R. J.: Rethinking the global secondary organic aerosol (SOA) budget: stronger
1297 production, faster removal, shorter lifetime, Atmos. Chem. Phys., 16, 7917-7941,
1298 https://doi.org/10.5194/acp-16-7917-2016, 2016.

1299 Hoesly, R. M., Smith, S. J., Feng, L., Klimont, Z., Janssens-Maenhout, G., Pitkanen, T.,
1300 Seibert, J. J., Vu, L., Andres, R. J., Bolt, R. M., Bond, T. C., Dawidowski, L., Kholod, N.,
1301 Kurokawa, J.-I., Li, M., Liu, L., Lu, Z., Moura, M. C. P., O'Rourke, P. R., and Zhang, Q.:
1302 Historical (1750–2014) anthropogenic emissions of reactive gases and aerosols from the
1303 Community Emissions Data System (CEDS), Geosci. Model Dev., 11, 369–408,
1304 https://doi.org/10.5194/gmd-11-369-2018, 2018.

1305 Huang, K., Fu, J. S., Prikhodko, V. Y., Storey, J. M., Romanov, A., Hodson, E. L., Cresko,
1306 J., Morozova, I., Ignatieva, Y., and Cabaniss, J.: Russian anthropogenic black carbon:

Emission reconstruction and Arctic black carbon simulation, J. Geophys. Res. Atmos., 120, 11,306– 11,333, doi:10.1002/2015JD023358, 2015.

Hudson, P. K., Murphy, D. M., Cziczo, D. J., Thomson, D. S., de Gouw, J. A., Warneke, C., Holloway, J., Jost, H. J. and Hübler, G.: Biomass-burning particle measurements: Characteristics composition and chemical processing, J. Geophys. Res. D Atmos., 109(23), 1–11, doi:10.1029/2003JD004398, 2004.

Janssens-Maenhout, G., Crippa, M., Guizzardi, D., Dentener, F., Muntean, M., Pouliot, G., Keating, T., Zhang, Q., Kurokawa, J., Wankmüller, R., Denier van der Gon, H., Kuenen, J. J. P., Klimont, Z., Frost, G., Darras, S., Koffi, B., and Li, M.: HTAP_v2.2: a mosaic of regional and global emission grid maps for 2008 and 2010 to study hemispheric transport of air pollution, Atmos. Chem. Phys., 15, 11411–11432, https://doi.org/10.5194/acp-15-11411-2015, 2015.

Jimenez, J. L., Canagaratna, M. R., Donahue, N. M., Prevot, a. S. H., Zhang, Q., Kroll, J. H., DeCarlo, P. F., Allan, J. D., Coe, H., Ng, N. L., Aiken, a. C., Docherty, K. S., Ulbrich, I. M., Grieshop, A. P., Robinson, a. L., Duplissy, J., Smith, J. D., Wilson, K. R., Lanz, V. a., Hueglin, C., Sun, Y. L., Tian, J., Laaksonen, A., Raatikainen, T., Rautiainen, J., Vaattovaara, P., Ehn, M., Kulmala, M., Tomlinson, J. M., Collins, D. R., Cubison, M. J., Dunlea, E. J., Huffman, J. A., Onasch, T. B., Alfarra, M. R., Williams, P. I., Bower, K., Kondo, Y., Schneider, J., Drewnick, F., Borrmann, S., Weimer, S., Demerjian, K., Salcedo, D., Cottrell, L., Griffin, R., Takami, A., Miyoshi, T., Hatakeyama, S., Shimono, A., Sun, J. Y., Zhang, Y. M., Dzepina, K., Kimmel, J. R., Sueper, D., Jayne, J. T., Herndon, S. C., Trimborn, a. M., Williams, L. R., Wood, E. C., Middlebrook, A. M., Kolb, C. E., Baltensperger, U., Worsnop, D. R., Worsnop, D. R., Dunlea, J., Huffman, J. A., Onasch, T. B., Alfarra, M. R., Williams, P. I., Bower, K., Kondo, Y., Schneider, J., Drewnick, F., Borrmann, S., Weimer, S., Demerjian, K., Salcedo, D., Cottrell, L., Griffin, R., Takami, A., Miyoshi, T., Hatakeyama, S., Shimono, A., Sun, J. Y., Zhang, Y. M., Dzepina, K., Kimmel, J. R., Sueper, D., Jayne, J. T., Herndon, S. C., Trimborn, a. M., Williams, L. R., Wood, E. C., Middlebrook, A. M., Kolb, C. E., Baltensperger, U., Worsnop, D. R., Dunlea, E. J., et al.: Evolution of Organic Aerosols in the Atmosphere, Science 80., 326(5959), 1525–1529, doi:10.1126/science.1180353, 2009.

Jimenez, J.L., P. Campuzano-Jost, D.A. Day, B.A. Nault, D.J. Price, and J.C. Schroder: ATom: L2 Measurements from CU High-Resolution Aerosol Mass Spectrometer (HR-

AMS). ORNL DAAC, Oak Ridge, Tennessee, USA. https://doi.org/10.3334/ORNLDAAC/1716, 2019a.

Jimenez, J.L., et al.: Evaluating the Consistency of All Submicron Aerosol Mass Measurements (Total and Speciated) in the Atmospheric Tomography Mission (ATom), Abstract A31A-08, presented at 2019 Fall Meeting, AGU, San Francisco, CA, 9-13 Dec., 2019b.

Jolleys, M. D., Coe, H., McFiggans, G., Taylor, J. W., O'Shea, S. J., Le Breton, M., Bauguitte, S. J.-B., Moller, S., Di Carlo, P., Aruffo, E., Palmer, P. I., Lee, J. D., Percival, C. J. and Gallagher, M. W.: Properties and evolution of biomass burning organic aerosol from Canadian boreal forest fires, Atmos. Chem. Phys., 15(6), 3077–3095, doi:10.5194/acp-15-3077-2015, 2015.

Kaiser, J. W., Heil, A., Andreae, M. O., Benedetti, A., Chubarova, N., Jones, L., Morcrette, J.-J., Razinger, M., Schultz, M. G., Suttie, M., and van der Werf, G. R.: Biomass burning emissions estimated with a global fire assimilation system based on observed fire radiative power, Biogeosciences, 9, 527–554, https://doi.org/10.5194/bg-9-527-2012, https://www.biogeosciences.net/9/527/2012/, 2012.

Kanakidou, M., Seinfeld, J. H., Pandis, S. N., Barnes, I., Dentener, F. J., Facchini, M. C., Van Dingenen, R., Ervens, B., Nenes, A., Nielsen, C. J., Swietlicki, E., Putaud, J. P., Balkanski, Y., Fuzzi, S., Horth, J., Moortgat, G. K., Winterhalter, R., Myhre, C. E. L., Tsigaridis, K., Vignati, E., Stephanou, E. G., and Wilson, J.: Organic aerosol and global climate modelling: a review, Atmos. Chem. Phys., 5, 1053-1123, https://doi.org/10.5194/acp-5-1053-2005, 2005.

Katich, J. M., Samset, B. H., Paul Bui, T., Dollner, M., Froyd, K.D., Campuzano-Jost, P., Nault, B. A., Schroder, J. C., Weinzierl, B., Schwarz, J. P.: Strong Contrast in Remote Black Carbon Aerosol Loadings Between the Atlantic and Pacific Basins, J. Geophys. Res. Atmos., 123 (23), pages 13,386-13,395, https://doi.org/10.1029/2018JD029206, 2018.

Kim, M. J., G. A. Novak, M. C. Zoerb,M. Yang, B. W. Blomquist, B. J. Huebert, C. D. Cappa, and T. H. Bertram: Air-Sea exchange of biogenic volatile organic compounds and the impact on aerosol particle size distributions, Geophys. Res. Lett.,44, 3887–3896, doi:10.1002/2017GL072975, 2017.

1369   Klimont, Z., K. Kupiainen, C. Heyes, P. Purohit, J. Cofala, P. Rafaj, J. Borken-Kleefeld,
1370   and W. Schöpp,: Global anthropogenic emissions of particulate matter including black
1371   carbon, Atmos. Chem. Phys., 17(14), 8681-8723, doi: 10.5194/acp-17-8681-2017, 2017.

1372   Kodros, J. K., Cucinotta, R., Ridley, D. A., Wiedinmyer, C., and Pierce, J. R.: The aerosol
1373   radiative effects of uncontrolled combustion of domestic waste, Atmos. Chem. Phys., 16,
1374   6771-6784, https://doi.org/10.5194/acp-16-6771-2016, 2016.

1375   Krechmer, J.E., D. Pagonis, P.J. Ziemann, and J.L. Jimenez. Quantification of gas-wall
1376   partitioning in Teflon environmental chambers using rapid bursts of low-volatility oxidized
1377   species generated in-situ. Environmental Science and Technology, 50, 5757–5765,
1378   doi:10.1021/acs.est.6b00606, 2016.

1379   Kroll, J. H., Donahue, N. M., Jimenez, J. L., Kessler, S. H., Canagaratna, M. R., Wilson,
1380   K. R., Altieri, K. E., Mazzoleni, L. R., Wozniak, A. S., Bluhm, H., Mysak, E. R., Smith, J.
1381   D., Kolb, C. E. and Worsnop, D. R.: Carbon oxidation state as a metric for describing the
1382   chemistry of atmospheric organic aerosol., Nat. Chem., 3(2), 133–9,
1383   doi:10.1038/nchem.948, 2011.

1384   Laskin, A., Laskin, J., and Nizkorodov, S.: Chemistry of Atmospheric Brown Carbon,
1385   Chem. Rev. 2015, 115, 10, 4335-4382, 2015.

1386   Lee, A. K. Y., Willis, M. D., Healy, R. M., Onasch, T. B., and Abbatt, J. P. D.: Mixing state
1387   of carbonaceous aerosol in an urban environment: single particle characterization using
1388   the soot particle aerosol mass spectrometer (SP-AMS), Atmos. Chem. Phys., 15, 1823-
1389   1841, https://doi.org/10.5194/acp-15-1823-2015, 2015.

1390   Liao, J., K.D. Froyd, D.M. Murphy, F.N. Keutsch, G. Yu, P.O.Wennberg, J.St. Clair, J.D.
1391   Crounse, A. Wisthaler, T. Mikoviny, T.B. Ryerson, I.B. Pollack, J. Peischl, J.L. Jimenez,
1392   P. Campuzano Jost, D.A. Day, B.E. Anderson, L.D. Ziemba, D.R. Blake, S. Meinardi, G.
1393   Diskin. Airborne organosulfates measurements over the continental US. Journal of
1394   Geophysical Research-Atmospheres, 120, 2990–3005, doi:10.1002/2014JD022378,
1395   2015.

1396   Liu, H. Y., D. J. Jacob, I. Bey, and R. M. Yantosca: Constraints from Pb-210 and Be-7 on
1397   wet deposition and transport in a global three-dimensional chemical tracer model driven
1398   by assimilated meteorological fields, J. Geophys. Res., 106(D11), 12,109–12,128, 2001.

1399 Liu, X., Easter, R. C., Ghan, S. J., Zaveri, R., Rasch, P., Shi, X., Lamarque, J.-F.,
1400 Gettelman, A., Morrison, H., Vitt, F., Conley, A., Park, S., Neale, R., Hannay, C., Ekman,
1401 A. M. L., Hess, P., Mahowald, N., Collins, W., Iacono, M. J., Bretherton, C. S., Flanner, M.
1402 G., and Mitchell, D.: Toward a minimal representation of aerosols in climate models:
1403 description and evaluation in the Community Atmosphere Model CAM5, Geosci. Model
1404 Dev., 5, 709-739, https://doi.org/10.5194/gmd-5-709-2012, 2012.

1405 Marais, E. A., Jacob, D. J., Jimenez, J. L., Campuzano-Jost, P., Day, D. A., Hu, W.,
1406 Krechmer, J., Zhu, L., Kim, P. S., Miller, C. C., Fisher, J. A., Travis, K., Yu, K., Hanisco, T.
1407 F., Wolfe, G. M., Arkinson, H. L., Pye, H. O. T., Froyd, K. D., Liao, J., and McNeill, V. F.:
1408 Aqueous-phase mechanism for secondary organic aerosol formation from isoprene:
1409 application to the southeast United States and co-benefit of SO2 emission controls,
1410 Atmos. Chem. Phys., 16, 1603-1618, https://doi.org/10.5194/acp-16-1603-2016, 2016.

1411 Myhre, G., Samset, B. H., Schulz, M., Balkanski, Y., Bauer, S., Berntsen, T. K., Bian, H.,
1412 Bellouin, N., Chin, M., Diehl, T., Easter, R. C., Feichter, J., Ghan, S. J., Hauglustaine, D.,
1413 Iversen, T., Kinne, S., Kirkevåg, A., Lamarque, J.-F., Lin, G., Liu, X., Lund, M. T., Luo, G.,
1414 Ma, X., van Noije, T., Penner, J. E., Rasch, P. J., Ruiz, A., Seland, Ø., Skeie, R. B., Stier,
1415 P., Takemura, T., Tsigaridis, K., Wang, P., Wang, Z., Xu, L., Yu, H., Yu, F., Yoon, J.-H.,
1416 Zhang, K., Zhang, H., and Zhou, C.: Radiative forcing of the direct aerosol effect from
1417 AeroCom Phase II simulations, Atmos. Chem. Phys., 13, 1853-1877,
1418 https://doi.org/10.5194/acp-13-1853-2013, 2013.

1419 Mauderly, J. L., & Chow, J. C: Health Effects of Organic Aerosols, Inhalation Toxicology,
1420 20:3, 257-288, DOI: 10.1080/08958370701866008, 2008.

1421 Middlebrook, A. M., Murphy, D. M. and Thomson, D. S.: Observations of organic material
1422 in individual marine particles at Cape Grim during the First Aerosol Characterization
1423 Experiment (ACE 1), J. Geophys. Res. Atmos., 103(D13), 16475–16483,
1424 doi:10.1029/97JD03719, 1998.

1425 Murphy, D. M., Froyd, K. D., Bian, H., Brock, C. A., Dibb, J. E., DiGangi, J. P., Diskin, G.,
1426 Dollner, M., Kupc, A., Scheuer, E. M., Schill, G. P., Weinzierl, B., Williamson, C. J., and
1427 Yu, P.: The distribution of sea-salt aerosol in the global troposphere, Atmos. Chem. Phys.,
1428 19, 4093-4104, https://doi.org/10.5194/acp-19-4093-2019, 2019.

1429 Nault, B. A., Campuzano-Jost, P., Day, D. A., Schroder, J. C., Anderson, B., Beyersdorf,
1430 A. J., Blake, D. R., Brune, W. H., Choi, Y., Corr, C. A., de Gouw, J. A., Dibb, J., DiGangi,

J. P., Diskin, G. S., Fried, A., Huey, L. G., Kim, M. J., Knote, C. J., Lamb, K. D., Lee, T., Park, T., Pusede, S. E., Scheuer, E., Thornhill, K. L., Woo, J.-H., and Jimenez, J. L.: Secondary organic aerosol production from local emissions dominates the organic aerosol budget over Seoul, South Korea, during KORUS-AQ, Atmos. Chem. Phys., 18, 17769-17800, https://doi.org/10.5194/acp-18-17769-2018, 2018.

Ovadnevaite, J., Ceburnis, D., Canagaratna, M., Berresheim, H., Bialek, J., Martucci, G., Worsnop, D. R. and O'Dowd, C.: On the effect of wind speed on submicron sea salt mass concentrations and source fluxes, J. Geophys. Res. Atmos., 117(D16), 1–11, doi:10.1029/2011JD017379, 2012.

Pai, S. J., Heald, C. L., Pierce, J. R., Farina, S. C., Marais, E. A., Jimenez, J. L., Campuzano-Jost, P., Nault, B. A., Middlebrook, A. M., Coe, H., Shilling, J. E., Bahreini, R., Dingle, J. H., and Vu, K.: An evaluation of global organic aerosol schemes using airborne observations, Atmos. Chem. Phys. Discuss., https://doi.org/10.5194/acp-2019-331, in press, 2020.

Palm, B. B., de Sá, S. S., Day, D. A., Campuzano-Jost, P., Hu, W., Seco, R., Sjostedt, S. J., Park, J.-H., Guenther, A. B., Kim, S., Brito, J., Wurm, F., Artaxo, P., Thalman, R., Wang, J., Yee, L. D., Wernis, R., Isaacman-VanWertz, G., Goldstein, A. H., Liu, Y., Springston, S. R., Souza, R., Newburn, M. K., Alexander, M. L., Martin, S. T., and Jimenez, J. L.: Secondary organic aerosol formation from ambient air in an oxidation flow reactor in central Amazonia, Atmos. Chem. Phys., 18, 467–493, https://doi.org/10.5194/acp-18-467-2018, 2018.

Petters, M. D., Prenni, A. J., Kreidenweis, S. M., DeMott, P. J., Matsunaga, A., Lim, Y. B., and Ziemann, P. J. Chemical aging and the hydrophobic-to-hydrophilic conversion of carbonaceous aerosol, Geophys. Res. Lett., 33, L24806, doi:10.1029/2006GL027249, 2006.

Pye, H. O. T., Chan, A. W. H., Barkley, M. P., and Seinfeld, J. H.: Global modeling of organic aerosol: The importance of reactive nitrogen (NOx and NO_3), Atmos. Chem. Phys., 10, 11,261–11,276, doi:10.5194/acp-10-11261-2010, 2010.

Robinson, A. L., Donahue, N. M., Shrivastava, M. K., Weitkamp, E. A., Sage, A. M., Grieshop, A. P., Lane, T. E., Pandis, S. N., and Pierce, J. R.: Rethinking organic aerosols: Semivolatile emissions and photochemical aging, Science, 315, 1259–1262, 2007.

1462 Schroder, J. C., Campuzano-Jost, P., Day, D. A., Shah, V., Larson, K., Sommers, J. M.,
1463 Sullivan, A. P., Campos, T., Reeves, J. M., Hills, A., Hornbrook, R. S., Blake, N. J.,
1464 Scheuer, E., Guo, H., Fibiger, D. L., McDuffie, E. E., Hayes, P. L., Weber, R. J., Dibb, J.
1465 E., Apel, E. C., Jaeglé, L., Brown, S. S., Thornton, J. A. and Jimenez, J. L.: Sources and
1466 Secondary Production of Organic Aerosols in the Northeastern United States during
1467 WINTER, J. Geophys. Res. Atmos., 123(14), 7771–7796, doi:10.1029/2018JD028475,
1468 2018.

1469 Schacht, J., Heinold, B., Quaas, J., Backman, J., Cherian, R., Ehrlich, A., Herber, A.,
1470 Huang, W. T. K., Kondo, Y. Massling, A, Sinha, P.R., Weinzierl, B. Zanatta, M., and Tegen,
1471 I.: The importance of the representation of air pollution emissions for the modeled
1472 distribution and radiative effects of black carbon in the Arctic, Atmos. Chem. Phys.
1473 Discuss., 2019, 1-39, doi: 10.5194/acp-2019-71, 2019.

1474 Schulz, M., Chin, M., and Kinne, S.: The aerosol model comparison project, AeroCom,
1475 phase II: clearing up diversity, IGAC newsletter, No. 41, 2–11, 2009.

1476 Scott, C. E., Rap, A., Spracklen, D. V., Forster, P. M., Carslaw, K. S., Mann, G. W., Pringle,
1477 K. J., Kivekäs, N., Kulmala, M., Lihavainen, H., and Tunved, P.: The direct and indirect
1478 radiative effects of biogenic secondary organic aerosol, Atmos. Chem. Phys., 14, 447-
1479 470, https://doi.org/10.5194/acp-14-447-2014, 2014.

1480 Shah, V., Jaeglé, L., Jimenez, J. L., Schroder, J. C., Campuzano-Jost, P., Campos, T. L.,
1481 et al.: Widespread pollution from secondary sources of organic aerosols during winter in
1482 the Northeastern United States. Geophysical Research Letters, 46, 2974– 2983.
1483 https://doi.org/10.1029/2018GL081530, 2019.

1484 Shiraiwa, M., Ueda, K., Pozzer, A., Lammel, G., Kampf, C. J.: Aerosol Health Effects from
1485 Molecular to Global Scales, Environ. Sci. Technol. 51 (23), pp 13545–13567, 2017.

1486 Shrivastava, M., Cappa, C.D., Fan, J., et al: Recent advances in understanding secondary
1487 organic aerosol: Implications for global climate forcing, Rev. Geophys., 55, 509–559,
1488 doi:10.1002/2016RG000540, 2017.

1489 Spracklen, D. V., Jimenez, J. L., Carslaw, K. S., Worsnop, D. R., Evans, M. J., Mann, G.
1490 W., Zhang, Q., Canagaratna, M. R., Allan, J., Coe, H., McFiggans, G., Rap, A., and
1491 Forster, P.: Aerosol mass spectrometer constraint on the global secondary organic aerosol
1492 budget, Atmos. Chem. Phys., 11, 12109–12136, doi:10.5194/acp-11-12109-2011, 2011.

1493 Tegen, I., Neubauer, D., Ferrachat, S., Siegenthaler-Le Drian, C., Bey, I., Schutgens, N.,
1494 Stier, P., Watson-Parris, D., Stanelle, T., Schmidt, H., Rast, S., Kokkola, H., Schultz, M.,
1495 Schroeder, S., Daskalakis, N., Barthel, S., Heinold, B., and Lohmann, U.: The global
1496 aerosol–climate model ECHAM6.3–HAM2.3 – Part 1: Aerosol evaluation, Geosci. Model
1497 Dev., 12, 1643-1677, https://doi.org/10.5194/gmd-12-1643-2019, 2019.

1498 Thomson, D. S., Schein, M. E. and Murphy, D. M.: Particle Analysis by Laser Mass
1499 Spectrometry WB-57F Instrument Overview, Aerosol Sci. Technol., 33(1–2), 153–169,
1500 doi:10.1080/027868200410903, 2000.

1501 Tilmes, S., Hodzic, A., Emmons, L.K., Mills, M.J., Gettelman, A., Kinnison, D.E., Park, M.,
1502 Lamarque J.-F., Vitt, F., et al.: Climate forcing and trends of organic aerosols in the
1503 Community Earth System Model (CESM2), to be submitted to JAMES, 2019.

1504 Tsigaridis, K., Daskalakis, N., Kanakidou, M., Adams, P. J., Artaxo, P., Bahadur, R.,
1505 Balkanski, Y., Bauer, S. E., Bellouin, N., Benedetti, A., Bergman, T., Berntsen, T. K.,
1506 Beukes, J. P., Bian, H., Carslaw, K. S., Chin, M., Curci, G., Diehl, T., Easter, R. C., Ghan,
1507 S. J., Gong, S. L., Hodzic, A., Hoyle, C. R., Iversen, T., Jathar, S., Jimenez, J. L., Kaiser,
1508 J. W., Kirkevåg, A., Koch, D., Kokkola, H., Lee, Y. H., Lin, G., Liu, X., Luo, G., Ma, X.,
1509 Mann, G. W., Mihalopoulos, N., Morcrette, J.-J., Müller, J.-F., Myhre, G., Myriokefalitakis,
1510 S., Ng, N. L., O'Donnell, D., Penner, J. E., Pozzoli, L., Pringle, K. J., Russell, L. M., Schulz,
1511 M., Sciare, J., Seland, Ø., Shindell, D. T., Sillman, S., Skeie, R. B., Spracklen, D.,
1512 Stavrakou, T., Steenrod, S. D., Takemura, T., Tiitta, P., Tilmes, S., Tost, H., van Noije, T.,
1513 van Zyl, P. G., von Salzen, K., Yu, F., Wang, Z., Wang, Z., Zaveri, R. A., Zhang, H., Zhang,
1514 K., Zhang, Q., and Zhang, X.: The AeroCom evaluation and intercomparison of organic
1515 aerosol in global models, Atmos. Chem. Phys., 14, 10845–10895, doi:10.5194/acp-14-
1516 10845-2014, 2014.

1517 Tsigaridis, K., and Kanakidou, M.: The Present and Future of Secondary Organic Aerosol
1518 Direct Forcing on Climate, Current Climate Change Reports, 2018, Volume 4, Issue 2, pp
1519 84–98, 2018.

1520 Turpin, B. J. and Lim, H. J.: Species contributions to PM2.5 mass concentrations:
1521 Revisiting common assumptions for estimating organic mass, Aerosol Sci. Tech., 35, 602–
1522 610, doi:10.1080/02786820152051454, 2001.

1523 Ulbrich, I. M., Canagaratna, M. R., Zhang, Q., Worsnop, D. R. and Jimenez, J. L.:
1524 Interpretation of organic components from Positive Matrix Factorization of aerosol mass

1525   spectrometric data, Atmos. Chem. Phys., 9(9), 2891–2918, doi:10.5194/acp-9-2891-2009,
1526   2009.

1527   van der Werf, G. R., Randerson, J. T., Giglio, L., Collatz, G. J., Mu, M., Kasibhatla, P. S.,
1528   Morton, D. C., DeFries, R. S., Jin, Y., and van Leeuwen, T. T.: Global fire emissions and
1529   the contribution of deforestation, savanna, forest, agricultural, and peat fires (1997–2009),
1530   Atmos. Chem. Phys., 10, 11707-11735, https://doi.org/10.5194/acp-10-11707-2010,
1531   2010.

1532   Vergara-Temprado, J., Murray, B. J., Wilson, T. W., O'Sullivan, D., Browse, J., Pringle, K.
1533   J., Ardon-Dryer, K., Bertram, A. K., Burrows, S. M., Ceburnis, D., DeMott, P. J., Mason,
1534   R. H., O'Dowd, C. D., Rinaldi, M., and Carslaw, K. S.: Contribution of feldspar and marine
1535   organic aerosols to global ice nucleating particle concentrations, Atmos. Chem. Phys., 17,
1536   3637-3658, https://doi.org/10.5194/acp-17-3637-2017, 2017.

1537   Wang, J., Cubison, M. J., Aiken, A. C., Jimenez, J. L., and Collins, D. R.: The importance
1538   of aerosol mixing state and size-resolved composition on CCN concentration and the
1539   variation of the importance with atmospheric aging of aerosols, Atmos. Chem. Phys., 10,
1540   7267-7283, https://doi.org/10.5194/acp-10-7267-2010, 2010.

1541   Williamson, C. J., Kupc, A., Axisa, D., Bilsback, K.R., Bui, T., Campuzano-Jost, P.,
1542   Dollner, M., Froyd, K., Hodshire, A. L., Jimenez, J. L., Kodros, J. K., Luo, G., Murphy, D.
1543   M., Nault, B. A., Ray, E. A., Weinzierl, B. B., Wilson, J. C., Yu, F., Yu, P., Pierce, J.F.,
1544   Brock C. A.: A Large Source of Cloud Condensation Nuclei from New Particle Formation
1545   in the Tropics, Nature, 574, https://doi.org/10.1038/s41586-019-1638-9, 2019.

1546   Wofsy, S.C., S. Afshar, H.M. Allen, E. Apel, E.C. Asher, B. Barletta, J. Bent, H. Bian, B.C.
1547   Biggs, D.R. Blake, N. Blake, I. Bourgeois, C.A. Brock, W.H. Brune, J.W. Budney, T.P. Bui,
1548   A. Butler, P. Campuzano-Jost, C.S. Chang, M. Chin, R. Commane, G. Correa, J.D.
1549   Crounse, P. D. Cullis, B.C. Daube, D.A. Day, J.M. Dean-Day, J.E. Dibb, J.P. DiGangi,
1550   G.S. Diskin, M. Dollner, J.W. Elkins, F. Erdesz, A.M. Fiore, C.M. Flynn, K. Froyd, D.W.
1551   Gesler, S.R. Hall, T.F. Hanisco, R.A. Hannun, A.J. Hills, E.J. Hintsa, A. Hoffman, R.S.
1552   Hornbrook, L.G. Huey, S. Hughes, J.L. Jimenez, B.J. Johnson, J.M. Katich, R.F. Keeling,
1553   M.J. Kim, A. Kupc, L.R. Lait, J.-F. Lamarque, J. Liu, K. McKain, R.J. Mclaughlin, S.
1554   Meinardi, D.O. Miller, S.A. Montzka, F.L. Moore, E.J. Morgan, D.M. Murphy, L.T. Murray,
1555   B.A. Nault, J.A. Neuman, P.A. Newman, J.M. Nicely, X. Pan, W. Paplawsky, J. Peischl,
1556   M.J. Prather, D.J. Price, E. Ray, J.M. Reeves, M. Richardson, A.W. Rollins, K.H. Rosenlof,

T.B. Ryerson, E. Scheuer, G.P. Schill, J.C. Schroder, J.P. Schwarz, J.M. St.Clair, S.D. Steenrod, B.B. Stephens, S.A. Strode, C. Sweeney, D. Tanner, A.P. Teng, A.B. Thames, C.R. Thompson, K. Ullmann, P.R. Veres, N. Vieznor, N.L. Wagner, A. Watt, R. Weber, B. Weinzierl, P. Wennberg, C.J. Williamson, J.C. Wilson, G.M. Wolfe, C.T. Woods, and L.H. Zeng. 2018. ATom: Merged Atmospheric Chemistry, Trace Gases, and Aerosols. ORNL DAAC, Oak Ridge, Tennessee, USA. https://doi.org/10.3334/ORNLDAAC/1581, 2018.

Woody, M. C., Baker, K. R., Hayes, P. L., Jimenez, J. L., Koo, B., and Pye, H. O. T.: Understanding sources of organic aerosol during CalNex-2010 using the CMAQ-VBS, Atmos. Chem. Phys., 16, 4081-4100, https://doi.org/10.5194/acp-16-4081-2016, 2016.

Yu, P., O. B. Toon, C. G. Bardeen, M. J. Mills, T. Fan, J. M. English, and R. R. Neely, Evaluations of tropospheric aerosol properties simulated by the community earth system model with a sectional aerosol microphysics scheme, J. Adv. Model. Earth Syst.,7, 865–914, doi:10.1002/2014MS000421, 2015.

Yu, P., Froyd, K. D., Portmann, R. W., Toon, O. B., Freitas, S. R., Bardeen, C. G., et al.: Efficient in-cloud removal of aerosols by deep convection. Geophysical Research Letters, 46. https://doi.org/10.1029/2018GL080544, 2019.

Zhang, K., O'Donnell, D., Kazil, J., Stier, P., Kinne, S., Lohmann, U., Ferrachat, S., Croft, B., Quaas, J., Wan, H., Rast, S., and Feichter, J.: The global aerosol-climate model ECHAM-HAM, version 2: sensitivity to improvements in process representations, Atmos. Chem. Phys., 12, 8911-8949, https://doi.org/10.5194/acp-12-8911-2012, 2012.

Zhang, Q. J., Beekmann, M., Drewnick, F., Freutel, F., Schneider, J., Crippa, M., Prevot, A. S. H., Baltensperger, U., Poulain, L., Wiedensohler, A., Sciare, J., Gros, V., Borbon, A., Colomb, A., Michoud, V., Doussin, J.-F., Denier van der Gon, H. A. C., Haeffelin, M., Dupont, J.-C., Siour, G., Petetin, H., Bessagnet, B., Pandis, S. N., Hodzic, A., Sanchez, O., Honoré, C., and Perrussel, O., 2013. Formation of organic aerosol in the Paris region during the MEGAPOLI summer campaign: evaluation of the volatility-basis-set approach within the CHIMERE model, Atmos. Chem. Phys., 13, 5767-5790, doi:10.5194/acp-13-5767-2013.

Zhang, X., Cappa, C. D., Jathar, S. H., McVay, R. C., Ensberg, J. J., Kleeman, M. J., and Seinfeld, J. H.: Influence of vapor wall loss in laboratory chambers on yields of secondary organic aerosol, P. Natl. Acad. Sci. USA, 111, 5802–5807, 2014.

1588   Zhao, G., Chen, Y., Hopke, P.K., Holsen, T.M., Dhaniyala, S.: Characteristics of traffic-
1589   induced fugitive dust from unpaved roads, Aerosol Science and Technology, 51:11, 1324-
1590   1331, DOI: 10.1080/02786826.2017.1347251, 2017.

1591   Zhu, J., Penner, J. E., Yu, F., Sillman, S., Andreae, M., and Coe, H.: Organic aerosol
1592   nucleation, climate and land use change: Decrease in radiative forcing, Nature
1593   Communications, 10, Article No. 423, https://www.nature.com/articles/s41467-019-
1594   08407-7, 2019.

1595   Zotter, P., I. El-Haddad, Y. Zhang, P.L. Hayes, X. Zhang, Y.H. Lin, L. Wacker, J. Schnelle-
1596   Kreis, G. Abbaszade, R. Zimmermann, J.D. Surratt, R. Weber, J.L. Jimenez, S. Szidat, U.
1597   Baltensperger, A.S.H. Prévôt. Diurnal cycle of fossil and non-fossil carbon using
1598   radiocarbon analyses during CalNex. Journal of Geophysical Research-Atmospheres,
1599   119, 6818–6835, doi:10.1002/2013JD021114, 2014.

1600

1601 Tables

1602 Table 1: ATom global model configurations and their treatment of the most important processes affecting organic aerosols.

Models & horizontal res. & met. fields & config. reference	Aerosol module	Submicron size[6] OA (dust/sea salt)	SOA precursors[1]					SOA production	Emission	POA/POC (SOA/SOC)	Removal		
			ISO	MT	SQ	ANT	C>12				Standard[2]	Improved	Photolytic
CESM1-CARMA (1.9°lon x 2.5°lat) MERRA-2 (Yu et al. 2019)	20 bins	< 500 nm (< 800 nm)	x	x		x		Semi-volatile using VBS (Pye et al. 2010)	GAIS and GFED v3	1.8 (N/A)	x	For convective updrafts (Yu et al. 2019)[3]	
CESM2-DYN (0.9° lon x 1.25° lat) GEOS5 (Tilmes et al. 2019)	4 modes	< 270 nm (< 800 nm)	x	x	x	x	x	Semi-volatile using VBS (Hodzic et al. 2016)	CMIP6 and QFED v2.4	1.8 (N/A)	x	Water solubility of organic gases per Hodzic et al. (2014)	For SOA (Hodzic et al. 2016)
CESM2-SMP GEOS5 (0.9° lon x 1.25° lat) (Tilmes et al. 2019)	4 modes	< 270 nm (< 800 nm)	x	x		x		Non-volatile with prescribed mass yields for all precursors[4]	CMIP6 and QFED v2.4	1.8 (N/A)	x		
ECHAM6-HAM ECHAM6 (1.87°lon x1.87°lat) (Tegen et al. 2019)	7 modes	< 500 nm (< 500 nm)			x			Non-volatile with 15% prescribed mass yields (Dentener et al. 2006)	ECLIPSE[5] and GFAS	1.4 (1.4)	x		
GC12-REF (2° lon x 2.5° lat) GEOS-FP (Bey et al. 2001)	Bulk	Bulk (< 500 nm)	x	x	x	x		Semi-volatile using VBS (Pye et al. 2010); non-volatile isoprene-	CMIP6 and GFED v4	2.1 (N/A)	x	For convective updrafts per Wang et al. 2014	

Model	Aerosol	Size range						SOA scheme	Emissions	OM:OC	Removal	Convective / solubility	SOA
								SOA (Marais et al. 2016)					
GC12-DYN (2° lon x 2.5° lat) GEOS-FP (Bey et al. 2001)	Bulk	Bulk (< 500 nm)	x	x	x	x	x	Semi-volatile using VBS (Hodzic et al. 2016); non-volatile isoprene-SOA (Marais et al. 2016)	CMIP6 and GFED v4	2.1 (N/A)	x	For convective updrafts (Wang et al. 2014); Water solubility of organic gases (Hodzic et al. 2014)	For SOA (Hodzic et al. 2016)
GC10-TOMAS (5° lon x 4° lat) GEOS-FP (Kodros et al. 2016)	15 bins	< 316 nm (< 316 nm)		x		x		Non-Volatile using 10% mass yields for MT, 0.2 Tg SOA per Tg CO for anthropogenic emissions	EDGAR v4 and GFED v3	1.8 (1.8)	x	For convective updrafts (Wang et al. 2014)	
GEOS5 (0.5°lon x 0.625°lat) MERRA-2 (Bian et al. 2019)	Bulk	bulk (< 1 μm for dust, 500 nm for seasalt)	x	x		x		Non-Volatile, 10% mass yields for all precursors	HTAP and QFED v2.54	1.8 (1.8)	x		

(1) SOA precursors include isoprene (ISO), monoterpenes (MT), sesquiterpenes (SQ), anthropogenics (ANT) including aromatics such as benzene, toluene and xylene, as well as lumped shorter chain alkanes and alkenes; and higher molecular weight n-alkanes and n-alkenes (C>12).

(2) Standard removal includes dry deposition and sedimentation, as well as convective and large-scale scavenging of soluble organic gases and aerosols, and below-cloud scavenging of aerosols.

(3) A sensitivity simulation is performed with CESM1-CARMA without the improved scavenging in convective updrafts.

(4) 5% for lumped C<12 alkanes, 5% for lumped C<12 alkenes, 15% for aromatics, 4% for isoprene, 25% for monoterpenes.

(5) Anthropogenic BC emission are replaced in Russia with the dataset of Huang et al. (2015).

(6) Submicron size range (diameter) used in various models for comparison with the AMS data.

1612 Table 2: Comparison of observed and simulated OA concentrations along ATom-1 and
1613 ATom-2 flights for eight global model simulations and their ensemble. The results of the
1614 model ensemble are also indicated. The statistical indicators are calculated as normalized
1615 mean bias $NMB(\%) = 100 \times \sum_i (M_i - O_i)/\sum_i O_i$; normalized mean error $NME(\%) =$
1616 $100 \times \sum_i |(M_i - O_i)| / \sum_i O_i$; root mean square error $RMSE(\mu g\ m^{-3}) =$
1617 $\sqrt{(1/N)\sum_i (M_i - O_i)^2}$ and correlation coefficient (R^2) between modeled (M_i) and observed
1618 (O_i) data points. The mean of ATom-1 observations is ~0.23 μg m^{-3} and for ATom-2 is
1619 0.11 μg m^{-3}. Figure S4 shows the normalized mean bias for all individual ATom model
1620 simulations for various latitudinal regions and for both the Atlantic and Pacific basins.

Organic aerosols	Avg.Mod. (μg m^{-3})	NMB (%)	NME (%)	RMSE (μg m^{-3})	R^2	Avg.Mod. (μg m^{-3})	NMB (%)	NME (%)	RMSE (μg m^{-3})	R^2
Model	*ATom-1 scores (August 2016)*					*ATom-2 scores (February 2017)*				
AeroCom-II Ens.	0.400	74.2	127.3	0.560	0.31	0.254	137	175	0.278	0.38
AeroCom-II Sub.[1]	0.335	47.0	111	0.557	0.28	0.242	127	178	0.290	0.27
ATom Ensemble	0.239	-4.5	64.6	0.372	0.66	0.139	23	92.6	0.224	0.48
CESM2-DYN	0.268	4.6	83.7	0.867	0.47	0.140	25.6	111.7	0.317	0.36
CESM2-SMP	0.349	36.3	94.3	0.556	0.51	0.175	57.2	125.4	0.299	0.31
CESM1-CARMA	0.155	-33.2	93.8	0.603	0.12	0.131	22.6	119.6	0.244	0.31
ECHAM6-HAM	0.400	73.6	143.6	0.714	0.24	0.214	100	184.0	0.363	0.23
GC12-DYN	0.142	-32.6	79.4	0.560	0.16	0.174	14.7	96.6	0.312	0.39
GC12-REF	0.122	-43.0	76.5	0.536	0.18	0.147	3.6	96.3	0.292	0.35
GC10-TOMAS	0.218	-14.4	86.5	0.644	0.16	0.313	150.0	223.7	0.537	0.12
GEOS5	0.242	-5.4	86.6	0.975	0.38	0.084	-24.9	86.4	0.268	0.29

1621 (1) This is the subset of AeroCom-II model ensemble that includes only seven
1622 models that are similar to those that are included in the ATom ensemble (either
1623 the same model, or an older model version, or the same aerosol module).
1624 AeroCom-II Sub. incudes CAM5-MAM3, CCSM4-hem, ECHAM5-HAM2,

1625   GEOSChem-APM 8.2, GEOSChem 9, GISS-TOMAS and GMI (see Tsigaridis
1626   et al., 2014 for their description).

1627 Figures:
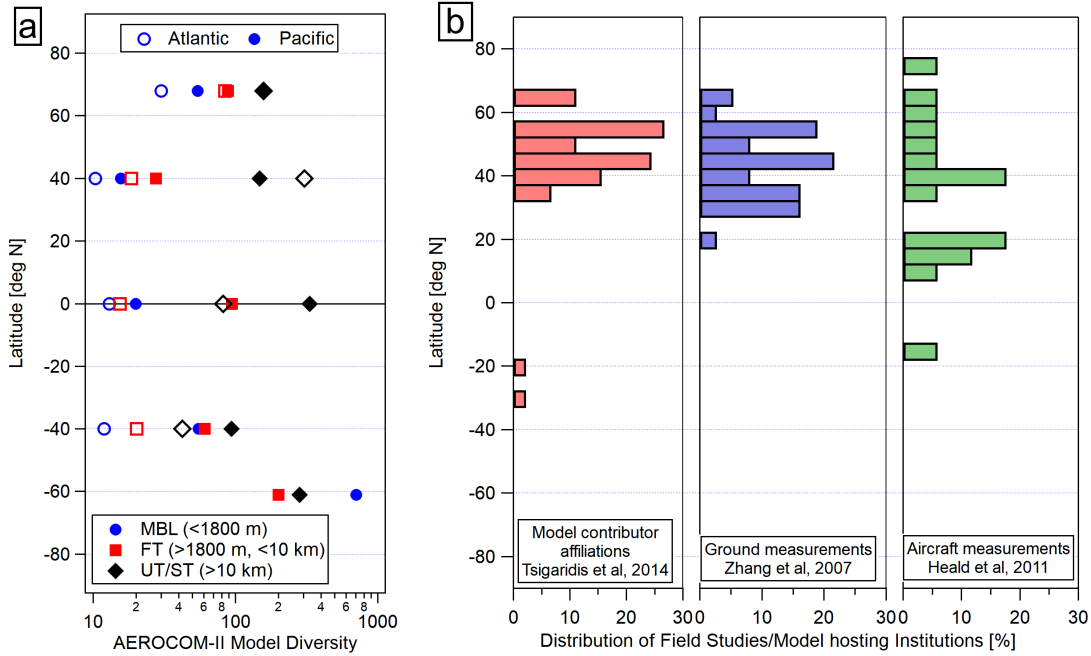
1628

1629 Figure 1: (a, left) The ratio between the average OA concentrations of the highest and the
1630 lowest models (for each region) as predicted among 28 global chemistry transport models
1631 participating in the AeroCom phase II intercomparison study (Tsigaridis et al. 2014); (b,
1632 right) Geographical distribution of institutions at which the AeroCom-II models were
1633 ran/developed (based on author affiliations) and of the field measurements included in two
1634 major literature overview studies (Zhang et al., 2007; Heald et al., 2011) for the OA ground
1635 and aircraft AMS as a function of latitude. For the aircraft campaigns, the average latitude
1636 for the full deployment was taken.

1637

1638

1639

1640

1641
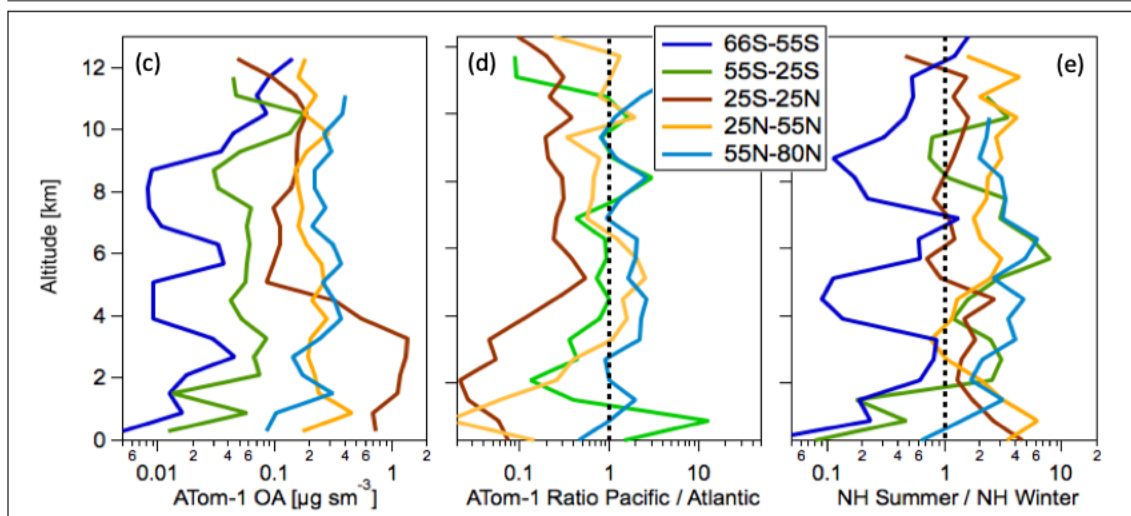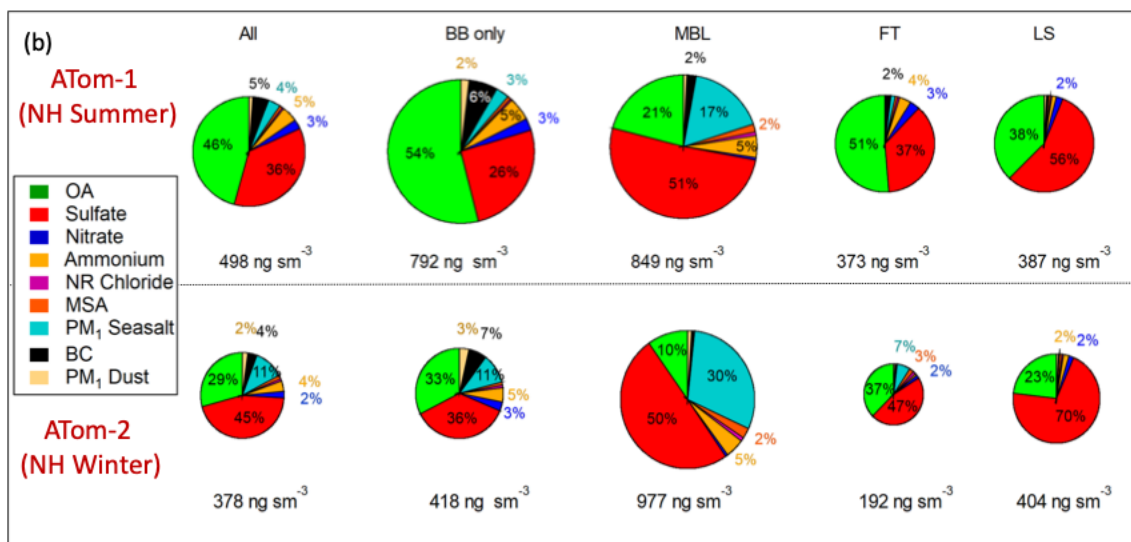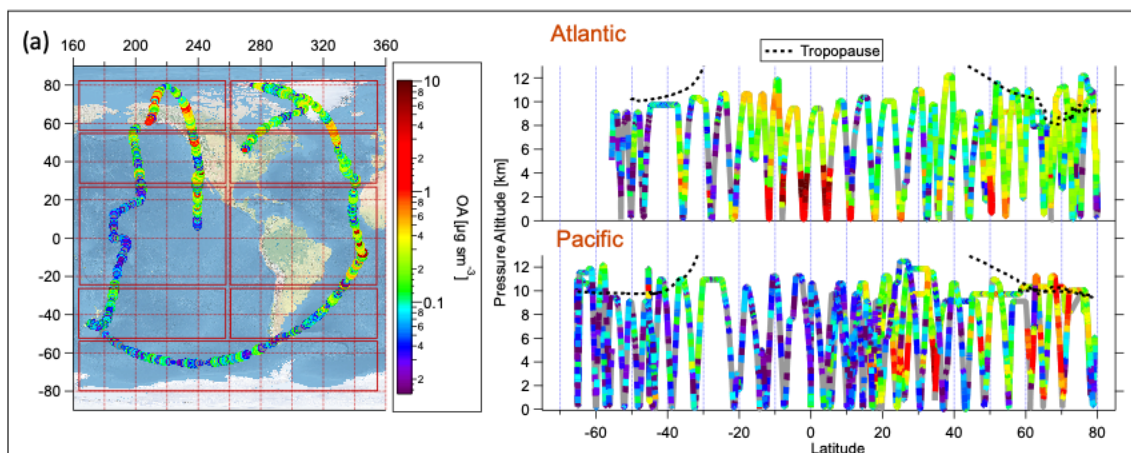
1642

1643 Figure 2: (a, left) ATom-1 DC-8 flights during the August 2016 deployment. Red boxes

1644 indicate regions used for the latitude averaging of the model results. (a, right) Vertical

1645 distribution of OA concentrations (μg sm^{-3}) along ATom-1 flight tracks (b) Average

1646 submicron aerosol composition as measured in the biomass-burning influenced regions

1647 (BB only), and the non-BB influenced regions including the marine boundary layer (MBL),

1648 free troposphere (FT), and lower stratosphere (LS) for ATom-1 (upper plots) and ATom-2

1649 (lower plots). The BB influenced airmasses were filtered using the PALMS data (see

1650 section 3.1). Contributions below 2% are shown but not labeled on the pie chart graph. In

1651 ATom-1, BB-only represents 24% of the data, clean MBL 8%, clean FT 57% and clean

1652 UT 12%, whereas in ATom-2 BB-only represents 3%, clean MBL 8%, clean FT 74%, clean

1653 UT 16%. (c) The average OA vertical profiles are shown for each latitude region as well

1654 as (d) the ratios between the Pacific and Atlantic Oceans in each region. (e) The seasonal

1655 contrast in OA concentrations as calculated as the ratio in OA concentrations between the

1656 NH summer (ATom-1) and NH winter (ATom-2) campaigns. The corresponding plots for

1657 ATom-2 can be found in Fig. S1.
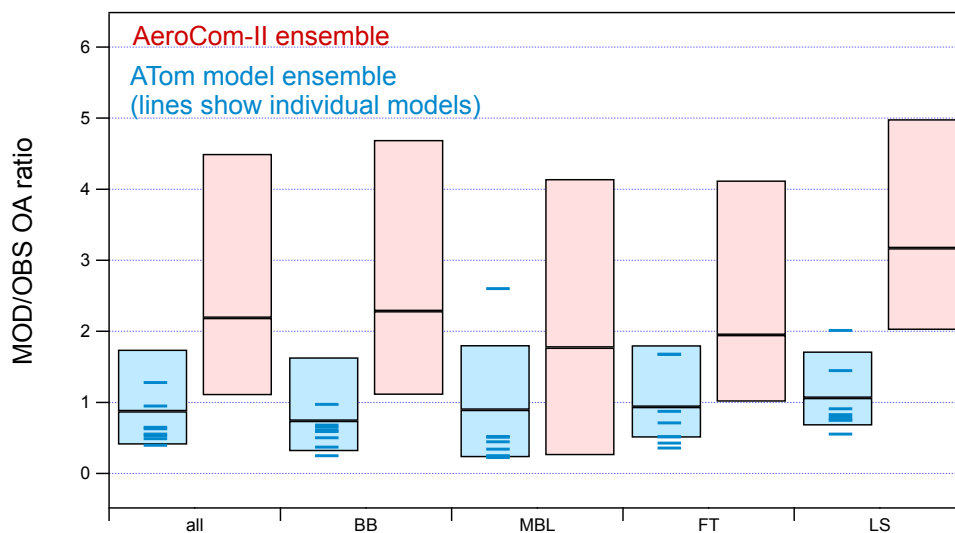
1658

1659 Figure 3: Ratios between predicted and observed OA concentrations for all ATom-1 flights

1660 as calculated for the ATom and AeroCom-II model ensembles in different regions ("BB"

1661 biomass burning influenced regions; "MBL" clean marine boundary layer; "FT" clean free

1662 troposphere' and "LS" lower stratosphere). Median of the ensemble ratio is shown as a

1663 horizontal line, while the boxes indicate 25th and 75th percentiles. Medians for the

1664 individual models included in the current ATom model ensemble are also shown as blue

1665 lines.
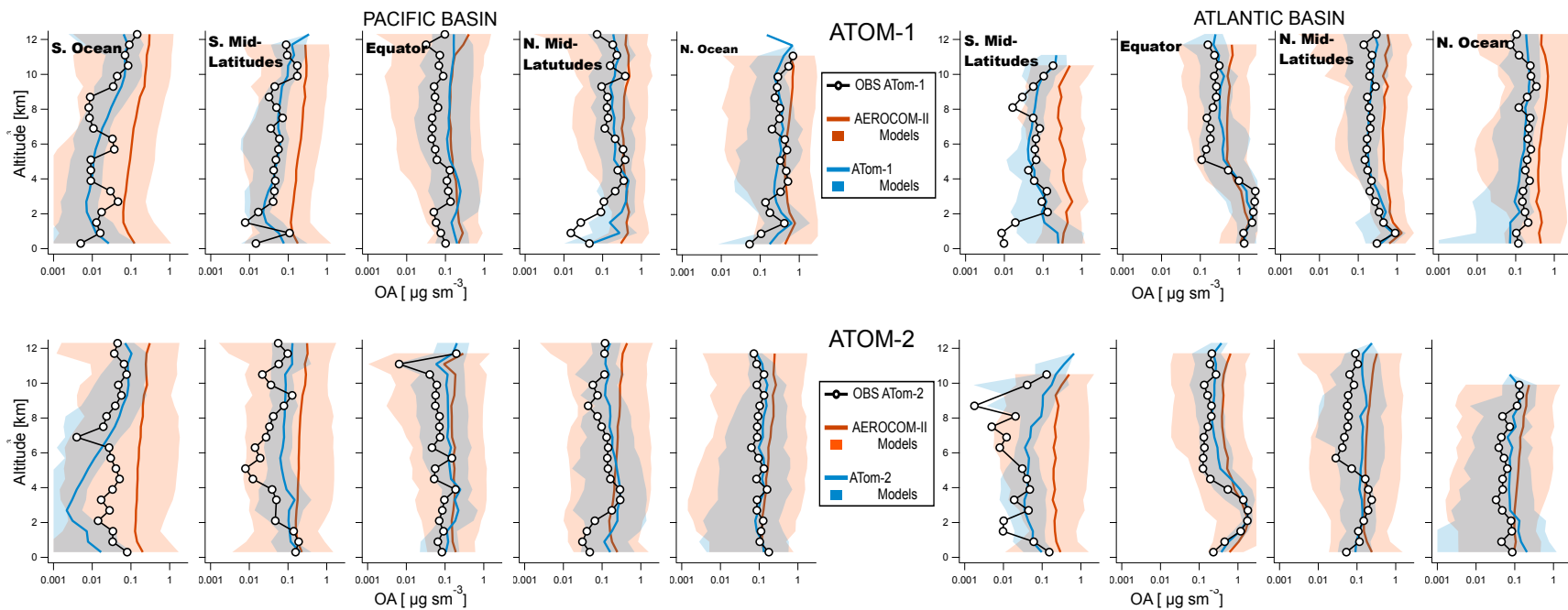
Figure 4: Comparison of latitude-averaged predicted OA vertical profiles with ATom-1 and -2 measurements taken over the Pacific (left side) and Atlantic (right side) basins. Results of the AeroCom-II model ensemble average are shown in red while those of the ATom model ensemble are shown in blue. Shaded areas indicate the variability (two standard deviations) within each model ensemble.

1671
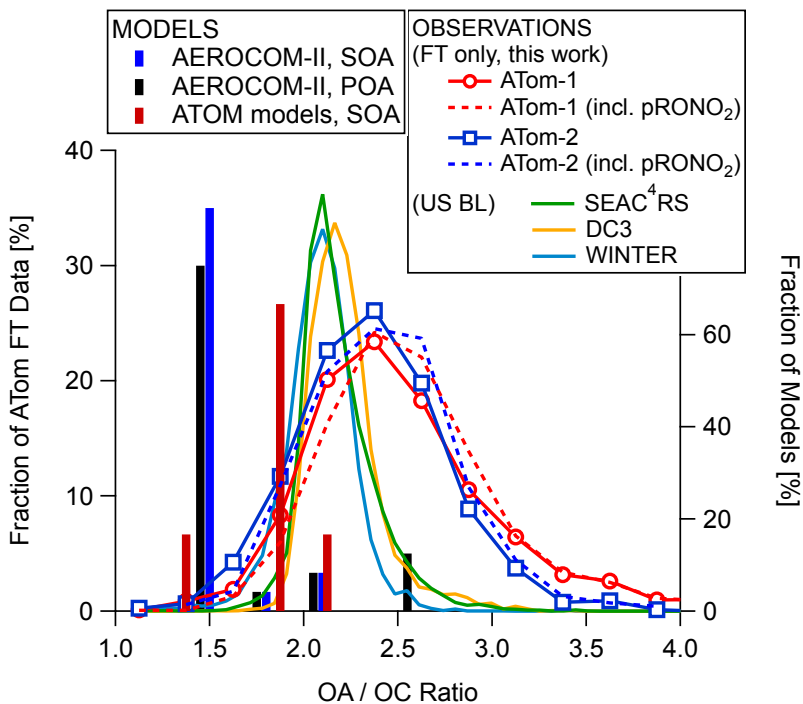
1672

Figure 5: Distribution of the OA / OC ratio as measured during ATom-1 and -2. Values for the recent aircraft campaigns (SEAC4RS, DC3 and WINTER) that took place over continental US regions closer to continental source regions are also shown (Schroder et al., 2018). The bars (right axis) show the OA/OC used for SOA and POA by the models included in the AeroCom and ATom ensemble, with OA/OC=1.4 being the modal value for the former and 1.8 for the latter.
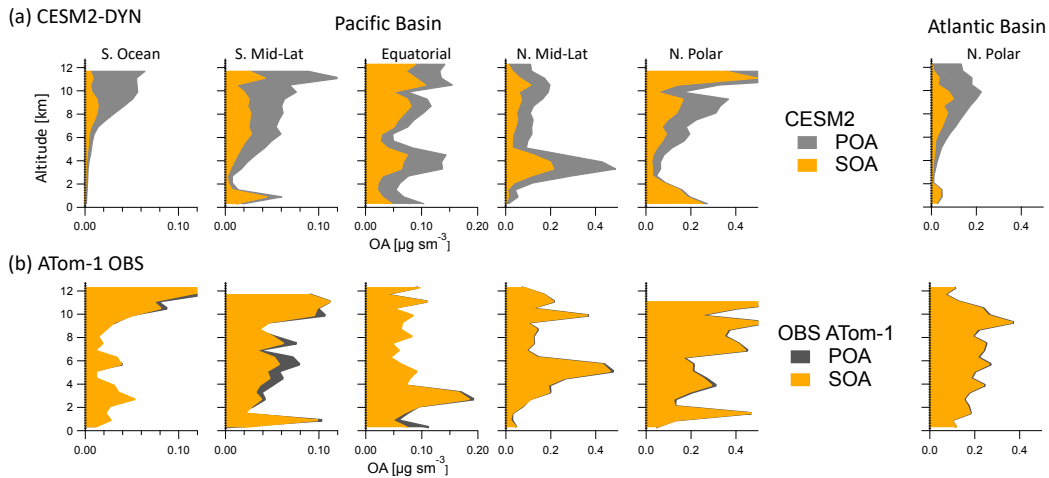
1679

Figure 6: Comparison of averaged POA and SOA vertical profiles as observed during ATom and as predicted by the CESM2-DYN model over the non-BB influenced Pacific and Atlantic basins. The comparison is not shown for the strongly biomass burning influenced regions as all the OA is conservatively allocated to POA in those regions.
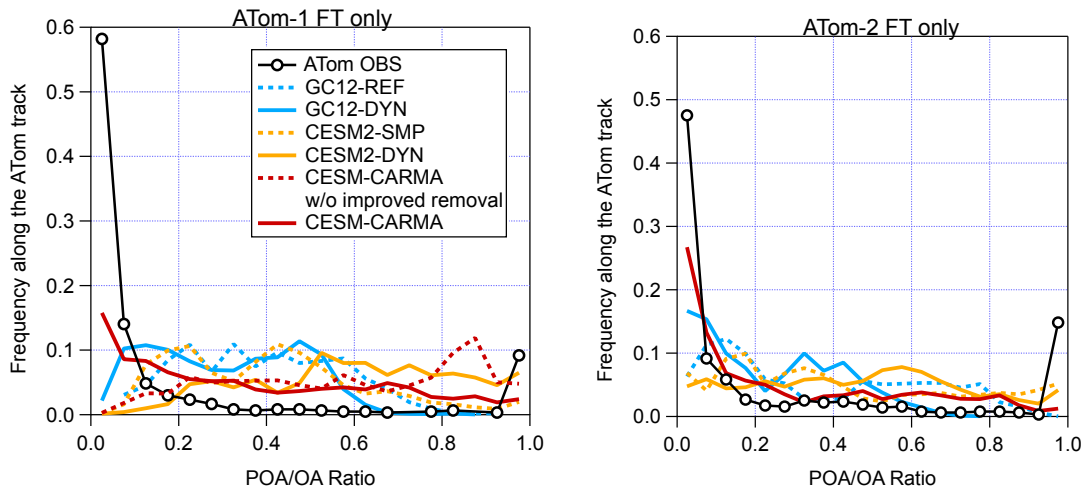
1684

Figure 7: Frequency distribution of observed and simulated ratio of POA to total OA in the free troposphere during ATom-1 and ATom-2 as computed by the GC12-, CESM2-, and CESM1-CARMA models.
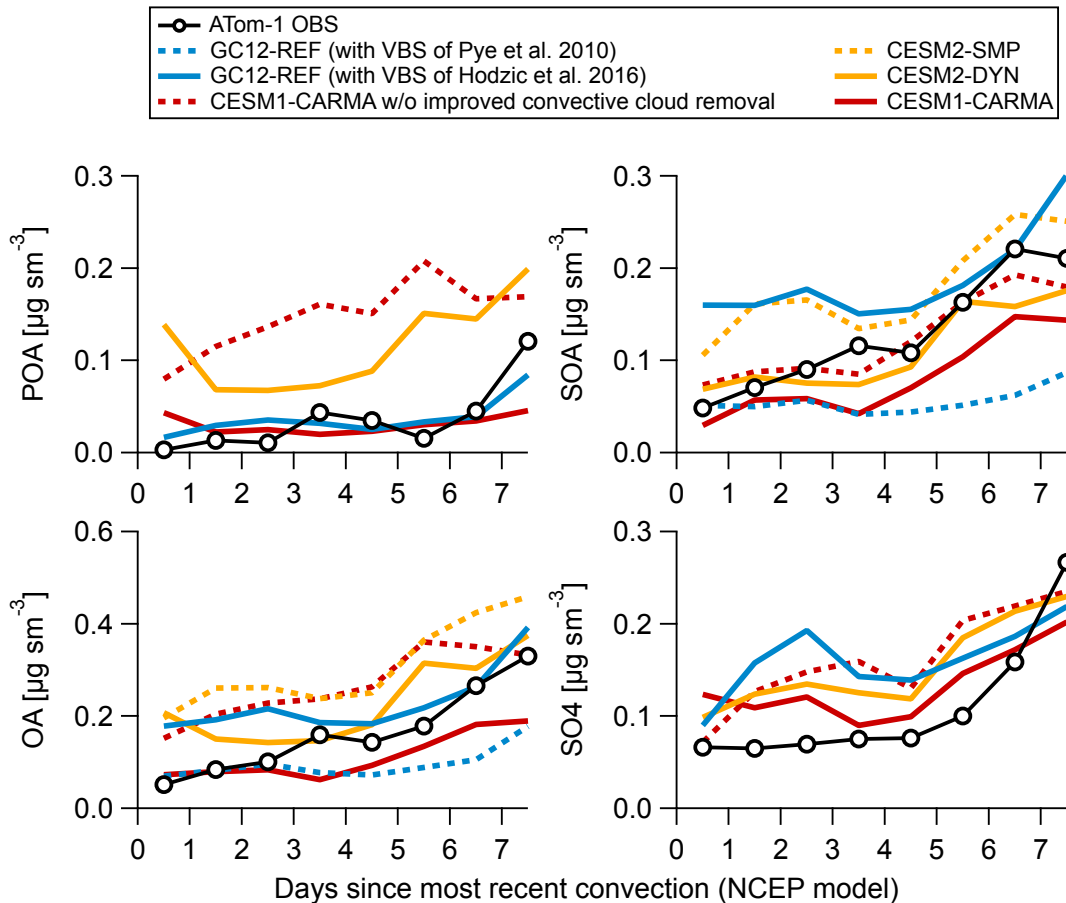
1688

Figure 8: Measured and predicted mass concentrations of POA, SOA, OA and sulfate aerosols during ATom-1 as a function of the number of days since the air mass was processed through convection (based on a trajectory model from Bowman, 1993, and satellite cloud data from NASA Langley, https://clouds.larc.nasa.gov/). CESM2-SMP and CESM2-DYN have the same emissions and processing of POA and sulfate, and thus similar concentrations. The same is true for the two versions of GC12.

1695

1696

1697

1698 (a)
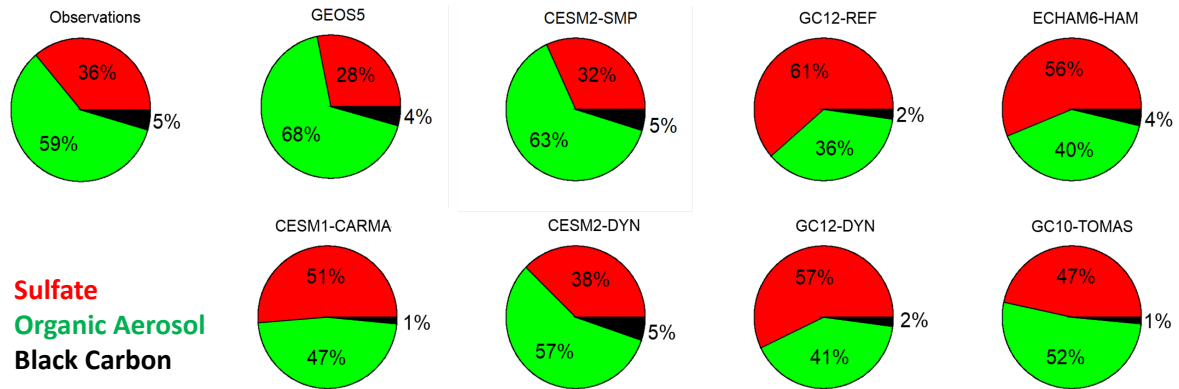
1699

1700 (b)
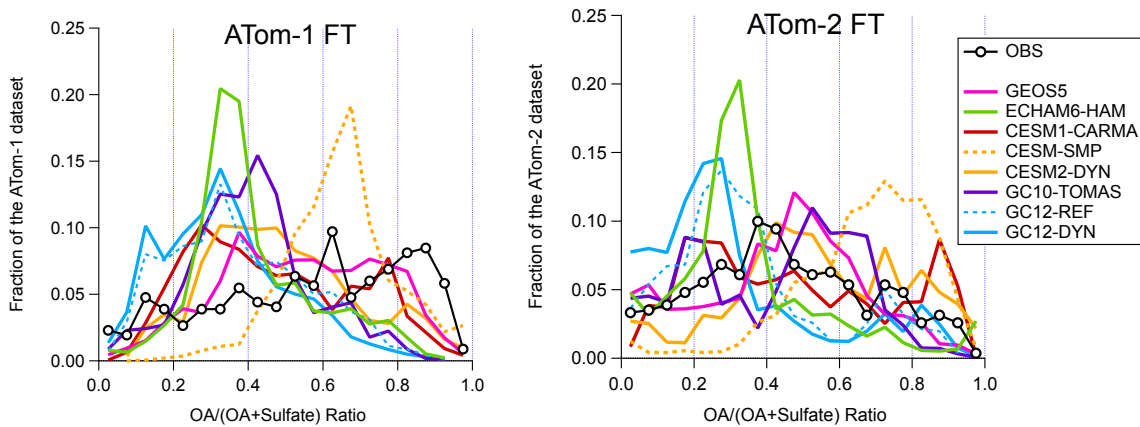
1701

1702 Figure 9: (a) Predicted and measured composition of submicron aerosols in the free
1703 troposphere as a function of the submicron aerosol mass concentrations during ATom-1.
1704 (b) Frequency distribution of observed and simulated ratio of organic to organic plus
1705 sulfate aerosols in the free troposphere during ATom-1 and -2.

1706

1707
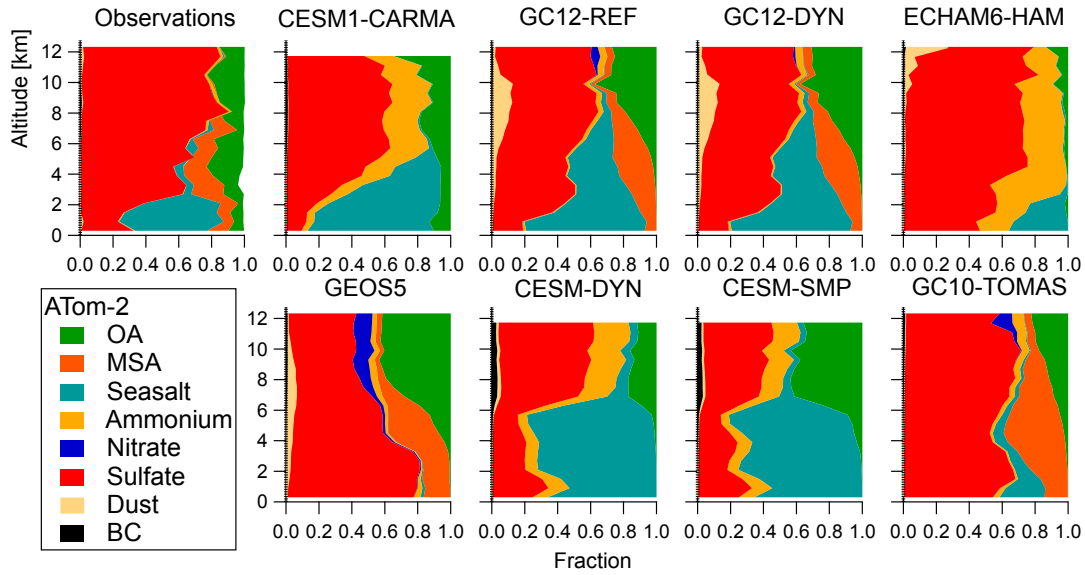
1710 Figure 10: Comparison of measured and predicted composition of submicron aerosols as
1711 a function of altitude over the remote Southern Ocean region during NH Winter (ATom-2).
1712 For models that do not calculate ammonium in the aerosol (such as CESM1-CARMA,
1713 CESM2-SMP, CESM2-DYN and ECHAM6-HAM), ammonium was estimated from the
1714 sulfate mass assuming the formation of ammonium sulfate. Note that while the modeled
1715 and measured submicron sea salt size ranges agree fairly well (Table 1), this is not quite
1716 the case for dust. Given that the accumulation mode dust in the models presented
1717 contains larger sizes than the AMS range (< 500 nm), it is expected for the modeled dust
1718 concentration to be larger than measured.

1719